SAND2022-6515J

A compact x-ray diffraction system for dynamic compression experiments on pulsed-power generators

T. Ao,[1,a] D.V. Morgan,[2] B.S. Stoltzfus,[1] K.N. Austin,[1]

J. Usher,[1] E. Breden,[1] L.M. Pacheco,[1] S. Dean,[1] J.L. Brown,[1] S. Duwal,[1] H. Fan,[1]

P. Kalita,[1] M.D. Knudson,[1] M. A. Rodriguez,[1] and J.M.D. Lane[1]

[1]Sandia National Laboratories, Albuquerque, NM 87185, USA

[2]Mission Support and Test Services, LLC, Albuquerque, NM 87185 USA

ABSTRACT

Pulsed-power generators can produce well-controlled continuous ramp compression of condensed matter for high-pressure equation-of-state studies using the magnetic loading technique. X-ray diffraction (XRD) data from dynamically compressed samples provide direct measurements of the elastic compression of the crystal lattice, onset of plastic flow, strength-strain rate dependence, structural phase transitions, and density of crystal defects such as dislocations. Here, we present a cost-effective, compact, pulsed x-ray source for XRD measurements on pulsed-power-driven ramp-loaded samples. This combination of magnetically-driven ramp compression of materials with a single, short-pulse XRD

---

[a] tao@sandia.gov

diagnostic will be a powerful capability for the dynamic materials community to investigate in situ dynamic phase transitions critical to equation-of-states. We present results using this new diagnostic to evaluate lattice compression in Zr and Al, and to capture signatures of phase transitions in CdS.

I. INTRODUCTION

Pulsed-power generators are able to create ramp compressed states with great uniformity, large size, and long duration [1, 2]. Historically, shock wave techniques have been used extensively to collect information on the high-pressure equation-of-state (EOS) of materials along the principal Hugoniot [3, 4, 5, 6]. The thermodynamic states produced by ramp loading of all materials, and solids in particular, are closer to the isentrope because entropy and heat producing shock fronts are avoided. The magnetic loading technique has been thoroughly developed on the pulsed-power generators at Sandia National Laboratories [7, 8, 9]. In this technique, samples are mounted on parallel flat conducting plates (anode and cathode). A direct short through the anode and cathode panels allows a 100-500 ns risetime current pulse to flow up one panel and down the other. The currents generate a planar time-varying magnetic field which induces strong shapeable Lorentz forces, pushing the anode and cathode apart. The resulting large magnetic pressure launches a high-pressure ramp wave from the conductor into the planar sample. The advantage of this approach over other techniques, such as graded-density gas gun impactors [10] and laser-driven ablation [11], is that a smooth, shockless compression can be achieved on large samples (0.1-1 mm thick, 10 mm diameter) over a long (hundreds of nanoseconds) duration.

One of the most fundamental properties of a crystalline solid is its lattice structure. Crystalline solid materials consist of atoms arranged in a definite, repeating pattern in three dimensions, called a Bravais (crystal) lattice [12]. The structure of a crystalline material may be represented geometrically by "Hermann–Mauguin notation" [13] which defines its symmetries in terms of point, plane, and space groups. Crystallographic planes are described using Miller indices (*hkl*), which are the integer coefficients of the reciprocal lattice vectors. In the process of x-ray diffraction (XRD), the momentum difference between incident and diffracted x-rays of a crystal is a reciprocal lattice vector. For an ideal monocrystalline material, the individual reciprocal lattice points are projected onto an x-ray detector as discrete peaks called "Laue spots" at associated diffraction angles. The locations of the measured peaks are used to determine the values of the (*hkl*) planes from which the x-rays were diffracted.

A polycrystalline material, or polycrystal, is made up of an aggregate of many small crystallites, or grains, each having a high degree of order. When a polycrystalline sample is illuminated by a monochromatic x-ray beam, each orientation reflects x-rays to a different location on a “Debye-Scherrer” cone [14, 15]. The Debye-Scherrer cone is the superset of the reflections formed by the crystal that satisfy Bragg’s Law. For a loose powder where nearly all orientations are represented, the reflections combine to form uniform cones of diffracted x-rays onto an x-ray detector called “Debye-Scherrer” rings. Unlike powders, polycrystals do not consist of randomly oriented crystallites. Rather, metal polycrystalline samples have grains of varying sizes and preferential orientations (texture), which tend to produce incomplete or spotty diffraction rings on the x-ray detector.

Although, in-situ dynamic XRD measurements have been performed on gas gun and laser compression platforms, implementation of XRD diagnostics on pulsed-power platforms has been challenging. Specifically, small gas gun and laser drivers have been built at large x-ray source facilities, such as the Dynamic Compression Sector (DCS) at the Advanced Photon Source (APS) [16, 17], and the Matter in Extreme Conditions (MEC) hutch at the Linac Coherent Light Source (LCLS) [18]. However, pulsed-power platforms are much harder to construct at these x-ray source facilities because of their large size and unique mode of operation. Moreover, the drive and sample geometries limit the use of transmission diffraction, due to the need for thick samples and high-Z materials. The reflection geometry for XRD is much more feasible on pulsed-power generators. These unique conditions require a custom on-site XRD design which is flexible and tailored to pulsed-power platforms.

The Thor machine is a recently constructed pulsed-power platform that enables unique ramp wave compression research [19]. Experimental loading paths can be finely controlled using Thor's precise pressure tailoring capability. The "Thor-XRD" diagnostic enables the mapping of high-pressure phase diagram of many materials of interest, and greatly expand the field of materials research by producing high quality *in-situ* measurements of materials under dynamic compression. Here, we have demonstrated an alternative and cost-effective approach of constructing a compact, pulsed-power x-ray source as a single-pulse XRD diagnostic for the Thor machine at Sandia National Laboratories. This compact flash x-ray diode system can generate a single, bright (~ 30 ns) pulse of narrow line emission (e.g., Mo-K-α, 17.4 keV, 0.71 Å) [20, 21] for use on Thor-XRD experiments, along with broadband bremsstrahlung emission up to 300 keV.

II. EXPERIMENTAL SETUP

a. Thor components and operation

The design and operation of the Thor machine has been thoroughly described by Reisman *et al.* [19], so only a brief overview is given here. Thor uses multiple capacitor-driven "brick" switches to deliver current to a power flow structure via impedance-matched, transit-time-isolated coaxial transmission cables. Each brick consists of a single switch and two capacitors connected electrically in series, with an inductance of 240 nH and a resistance of 0.37 Ω. The peak current for a ± 100 kV capacitor charge is 36 kA with a rise time of ~ 60 ns. The bricks can be individually triggered to achieve a high degree of current pulse tailoring. The resulting current is concentrated into a "strip-line" load where dynamic material experiments can be performed using the large magnetic pressures that are generated.

Figure 1 shows the overall layout of the Thor machine at Sandia's Dynamic Integrated Compression Experimental (DICE) Facility. Figure 1(a) shows the eight "brick towers" that each contain eight vertically stacked bricks. Also shown are the corresponding transmission cables (custom 10 Ω coaxial cables made by Dielectric Sciences Inc.) wrapped around "cable towers" for space management (~ 8 miles in total length) to fit in a 30'x50' space of 1,500 sqft. Figure 1(b) shows the cables feeding into the central power flow (CPF) structure that surrounds the load chamber where all of Thor's energy is discharged into the strip-line load. Presently, Thor is powered by 64 decoupled and transit-time isolated bricks with a total stored energy of 50 kJ, which can produce peak pressures of 10-30 GPa, depending on the pulse shape and load panel width.

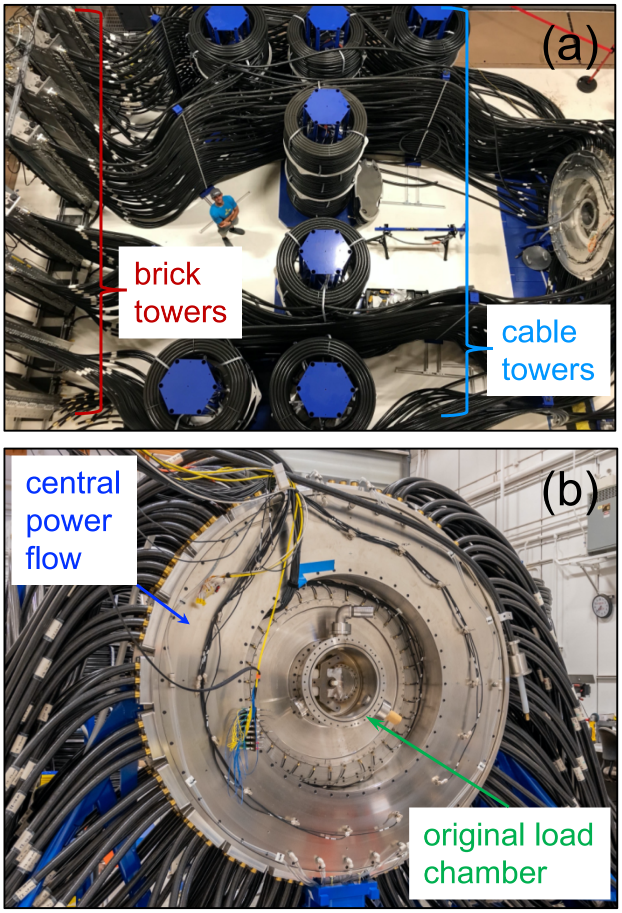

Figure 1. (a) Overhead photo of Thor's brick and cable towers. (b) Photo of Thor's central power flow structure and original load chamber.

Figure 2 shows schematics of typical strip-line load panels that have been fielded on Thor. These standard load panels have been fabricated from bulk pieces of either 6061-T6 aluminum (Al) or OFHC (oxygen-free high conductivity) copper (Cu) and consist of two main parts: a body and a base, as shown in the isometric view in Figure 2(a). The panel body was typically 30-50 mm in length and 10-20 mm in width. A cross-sectional view of the load region is shown in Figure 2(b).

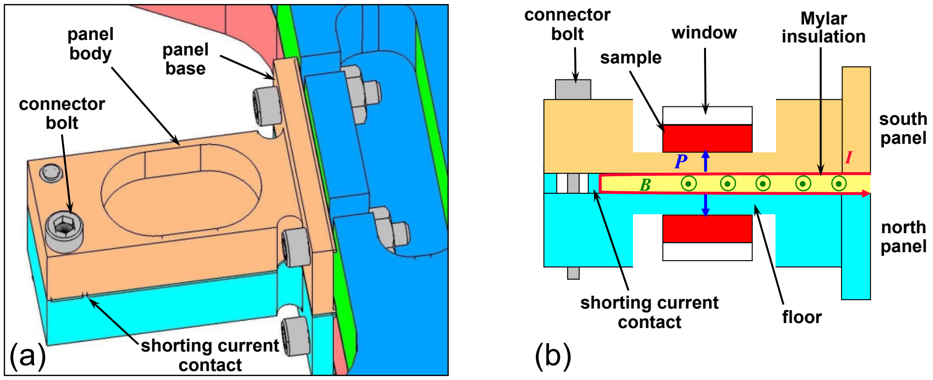

Figure 2. (a) An isometric view of the load panels. (b) A cross-section view of the load region which depicts the **J**×**B** force exerted on the load panels and samples.

To hold samples and windows, a pocket was machined into the panel body whose depth was defined by its floor thickness (0.5-1.5 mm thick). The two load panels (designated as “north” and “south”) were separated by several layers of Mylar insulator with a total thickness of 0.25 mm. The insulating Mylar constrains the current flow along the inner surfaces between the north and south panels through a shorting current contact. Within the gap between the panels, strong magnetic fields are set up perpendicular to the current path, and the resulting **J**×**B** force produces magnetic pressures on the panels given as

$$P = k_E \frac{B^2}{2\mu} = k_E \frac{\mu}{2}\left(\frac{I}{w}\right)^2. \tag{1}$$

The pressure, *P,* on the panels varies proportionately to the square of the current density, *J,* or current, *I,* divided by the panel width, *w*, where *B* is the magnetic field between the panels, μ is the magnetic permeability between the panels ($\mu_{Mylar} \approx \mu_0$, the magnetic permeability of free space), and k_E is an experimental scaling coefficient. The magnetic pressure at the inner panel surface initiates a hydrodynamic wave that propagates through the load panels and reaches the outer panel surface where samples are placed. For north and south load panels with identical materials and dimensions, the drive histories will be the same.

The load samples are typically 8-15 mm in diameter and 0.1-1 mm in thickness. A laser-grade window is glued onto the back surface of the sample to observe the sample/window interface while the sample remains pressurized. For the ramp compression experiments, velocimetry diagnostics, such as Velocity Interferometer System for Any Reflector (VISAR) [22, 23] and Photonic Doppler Velocimetry (PDV) [24, 25], are used to track the particle velocity profiles of the sample. For either VISAR or PDV measurements, the rear side of the load sample (either a free surface or through a transparent window) is illuminated with light from a laser through a “send” optical fiber. As the pressure wave propagates through the sample and reaches the reflecting interface, the motion of the sample results in Doppler shifting of the reflected light. The reflected light from the sample is collected by a corresponding “receive” optical fiber.

b. X-ray diffraction diagnostic

The cross-sectional schematic of Figure 3 shows the geometry of the input x-rays from the x-ray diode head to the load panels, and the diffracted x-rays recorded by the image plate (IP) x-ray detector. The current flows on the inner surfaces of load panels perpendicular to the plane of this view. The "XRD load" consists of a XRD sample and x-ray window glued to the south panel. The "drive load" consists of a PDV/VISAR window glued to the north panel.

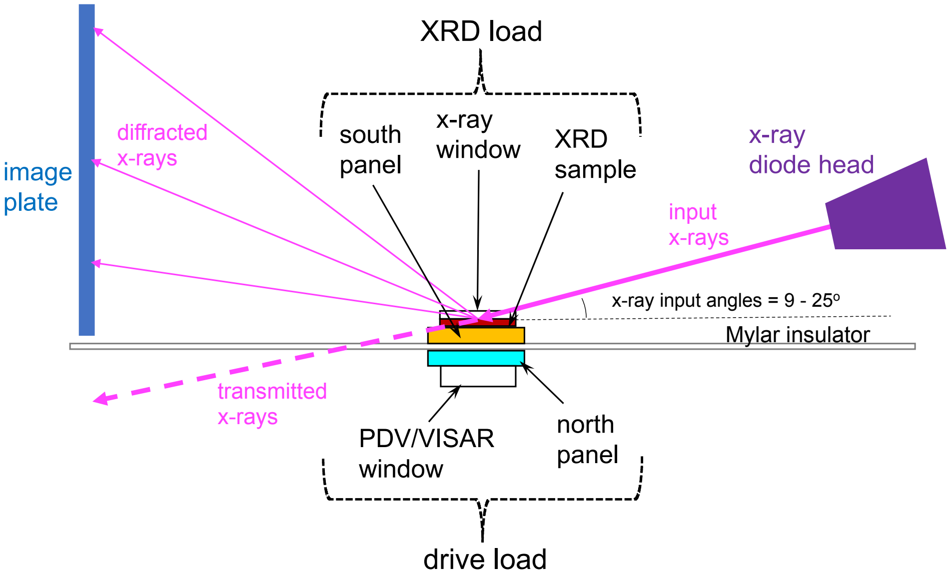

Figure 3. Cross-sectional schematic of Thor-XRD setup.

The x-ray source is based on the flash x-ray system described in detail by Morgan *et al.* [20], which consists of a 35-stage Marx bank high-voltage pulse generator coupled to a needle-and-washer electron beam diode via a 41 Ω, DS-2158 coaxial transmission cable. The Marx generator, coaxial transmission "feed cable", and coupling to the x-ray diode were all pressurized to 85 psi with dry air. The Marx bank's capacitor stages are charged to −30 kV and subsequently triggered to discharge in series into the remote needle-and-washer x-ray diode. Various electron beam diode systems have been developed to create high-brightness, flash x-ray radiography sources, but are optimized to produce bremsstrahlung radiation [26, 27, 28]. In contrast, this flash x-ray diode system was specially designed to produce line emission for XRD using a short, low-characteristic impedance vacuum transmission line section and a needle-and-washer anode-cathode (A-K) configuration. Specifically, a 3.8-mm-diameter aperture tungsten alloy (W-90%) cathode and 1.5-mm-diameter anode with a spherical tip were used, and all sharp points and edges in the A-K region were eliminated. This resulted in higher emission current and lower electron impact energy, thereby increasing the production of characteristic line emission, while minimizing broadband bremsstrahlung emission. In this configuration, the peak voltage across the diode was estimated to be about 300 kV.

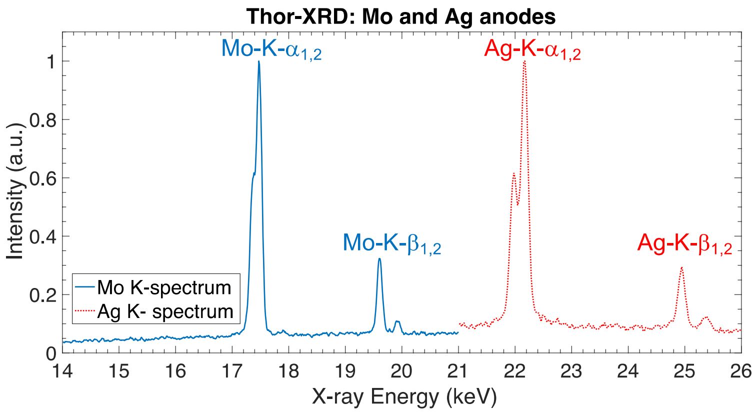

Figure 4. X-ray energy spectra generated by Mo and Ag anodes.

Figure 4 shows the x-ray energy spectrum for anodes composed of molybdenum (Mo) and silver (Ag). The flash x-ray diode operates by emitting electrons from the washer-cathode and accelerating them towards the needle-anode. Bremsstrahlung (continuum) radiation is produced when an electron undergoes strong deflection caused by deceleration. X-rays with discrete energies characteristic of the anode's element are also emitted when the anode is bombarded with high energy electrons. The energies of these "characteristic x-rays" are determined by the differences in these binding energies of atomic states. Generally, the brighter K-α line emission is used for the XRD measurements, and the weaker K-β line emission is minimized using filters.

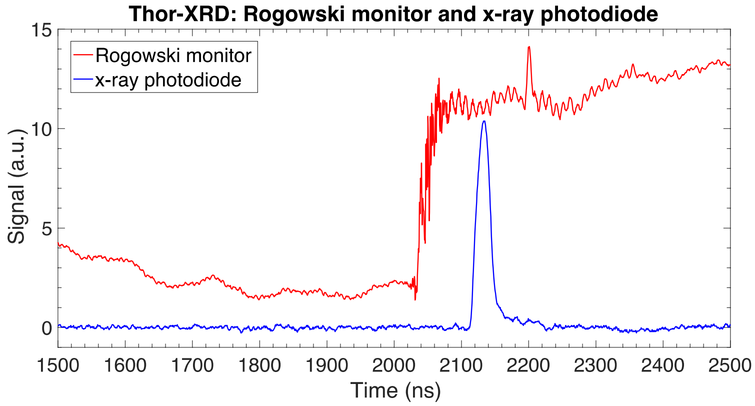

Figure 5. The firing of the Marx measured by the Rogowski monitor and the arrival of x-rays at the XRD sample measured by an x-ray photodiode placed at the XRD load.

To establish the timing of the x-ray pulse relative to the discharge of the Marx generator, an internal Rogowski monitor [29] within the Marx was used to generate a timing mark. An x-ray photodiode was temporarily placed at the XRD load panel to measure the arrival of x-rays at the XRD sample. Based on repeated firings of the Marx, an average delay of 100 ns between the Marx Rogowski monitor and x-ray photodiode peak signal was measured (see Figure 5).

To determine the x-ray timing for dynamic Thor-XRD experiments, the x-ray photodiode was removed and the Rogowski monitor signal was recorded. The flash x-ray diode system generates a single, bright (~30 ns) pulse of narrow line emission, as shown in Figure 6(a). During each firing of the x-ray diode, the electron beam degrades the anode.

Depending on the anode material, fewer line emission photons are produced on each subsequent shot until the anode must be replaced (i.e., Ag: 3-4 shots, Cu: 4-6 shots, Mo: 6-8 shots). However, the spectrum does not change significantly between shots. The shot-to-shot variation of the x-ray pulse was measured to be about ± 5 ns, as shown in Figure 6(b).

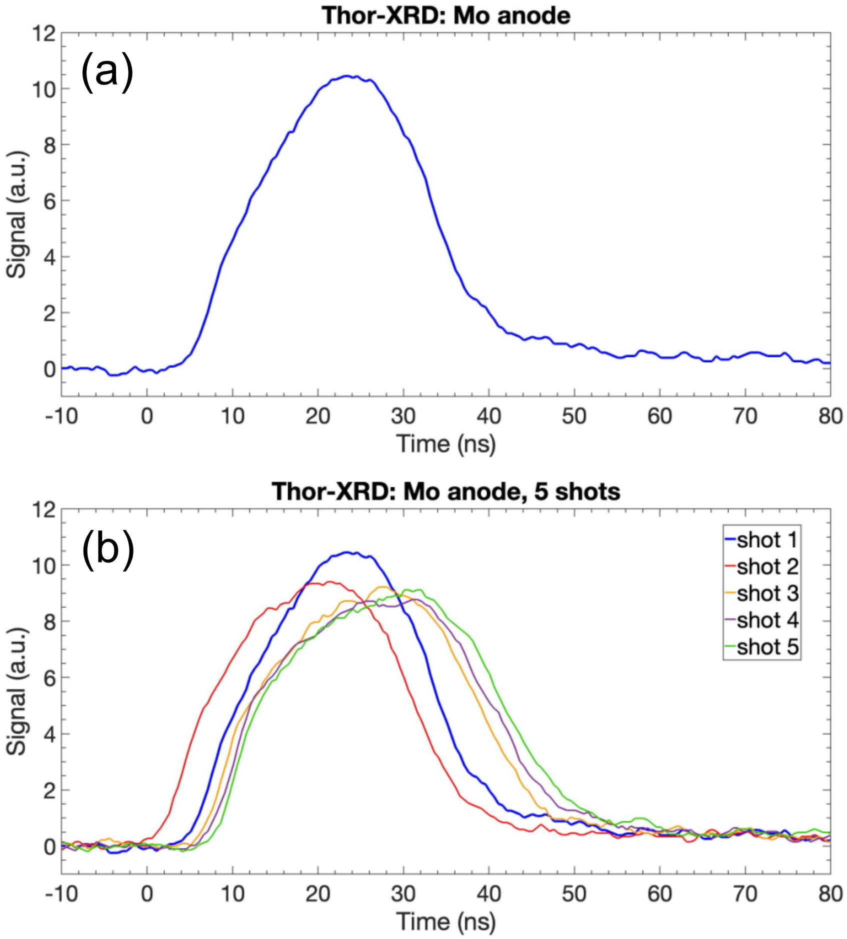

Figure 6. (a) X-ray photodiode measurement of the time history of a single x-ray pulse (FWHM ≈ 30 ns). (b) The shot-to-shot reproducibility of multiple x-ray pulses (jitter ≈ ± 5 ns).

A new conical x-ray diode head with a 90° bend in the vacuum transmission line was designed so that the diode and alignment fixture could be mounted directly to Thor's central power flow (CPF) feed plate. This configuration allowed placement of the tungsten slit collimator (1 mm wide by 2.5 mm tall) close to the sample, providing an angular beam divergence of about 0.5º in the horizontal symmetry plane, which is the plane defined by the input x-ray beam and the Thor drive pulse direction of propagation. Installation of this right-angle x-ray diode head within the Thor load chamber is shown in Figure 7.

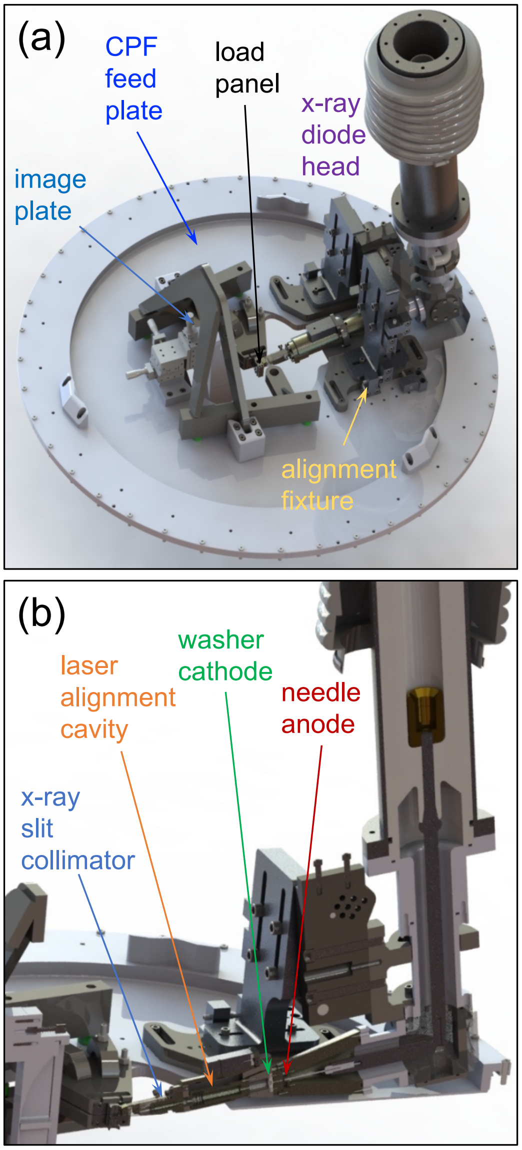

Figure 7. (a) Isometric rendering of Thor-XRD showing the CPF feed plate, right-angle x-ray diode head, alignment fixture, load panel, and image plate x-ray detector inside Thor load chamber. (b) Cross-sectional rendering of right-angle x-ray diode head showing needle anode, washer cathode, laser alignment cavity, and x-ray slit collimator.

The isometric rendering of Figure 7(a) shows how the x-ray diode head is mounted on the CPF feed plate relative to the load panel and IP x-ray detector. The right-angle x-ray diode head is adjustable to x-ray input angles between 9 and 25°. An input angle of 11° was selected for all of the results presented here to enable the XRD data at lower diffraction angles to be measured. The cross-sectional rendering of Figure 7(b) shows the locations of the needle anode and washer cathode inside the x-ray diode head, the laser alignment cavity, and the x-ray collimator next to the load panel. A removable alignment laser inside the laser alignment cavity is locked into a colinear configuration with respect to the x-ray beam, illuminating the target through the slit collimator. For the Thor-XRD experiment, the alignment laser is removed, and the cavity is shielded with a tungsten cover.

Since previous Thor experiments only fielded VISAR and PDV diagnostics that used flexible optical fibers, the original load chamber was designed to be relatively small (*i.e.,* ~ 40 cm in diameter and ~ 20 cm in depth) to be readily mounted and unmounted from the CPF feed plate (see Figure 1(b)). To accommodate the right-angle x-ray diode head a new expanded load chamber was designed and fabricated, as shown in Figure 8(a). This chamber measured ~ 95 cm in diameter and ~ 45 cm in depth. In addition, a new CPF feed plate was designed and fabricated for the Thor-XRD experiments. Figure 8(b) shows the Marx's feed cable connected to the right-angle x-ray diode head with the closed, expanded load chamber during a Thor-XRD experiment.

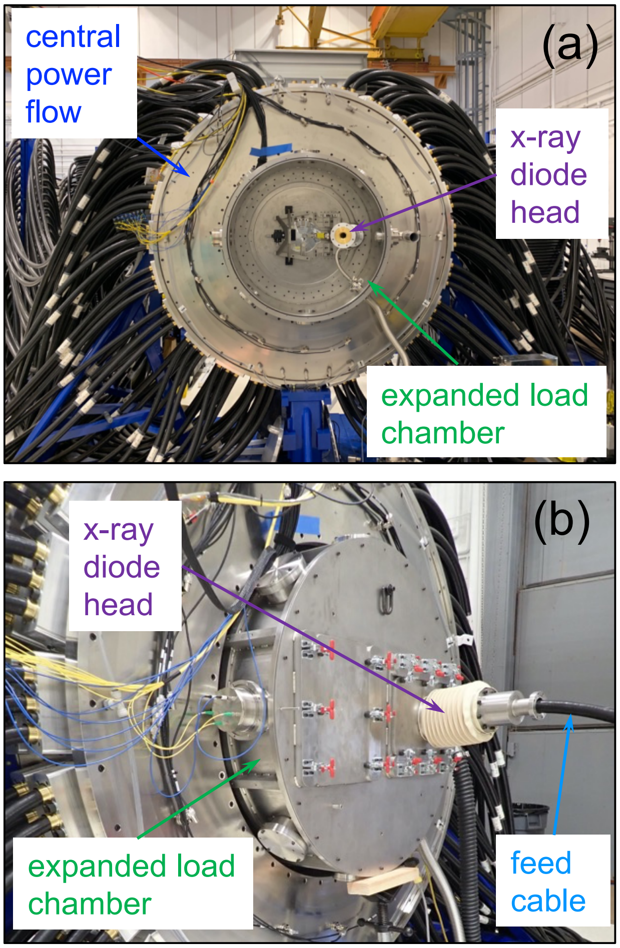

Figure 8. (a) Photo of central power flow with expanded load chamber right-angle x-ray diode. (b) Photo of closed expanded load chamber and feed cable connected to right-angle x-ray diode head.

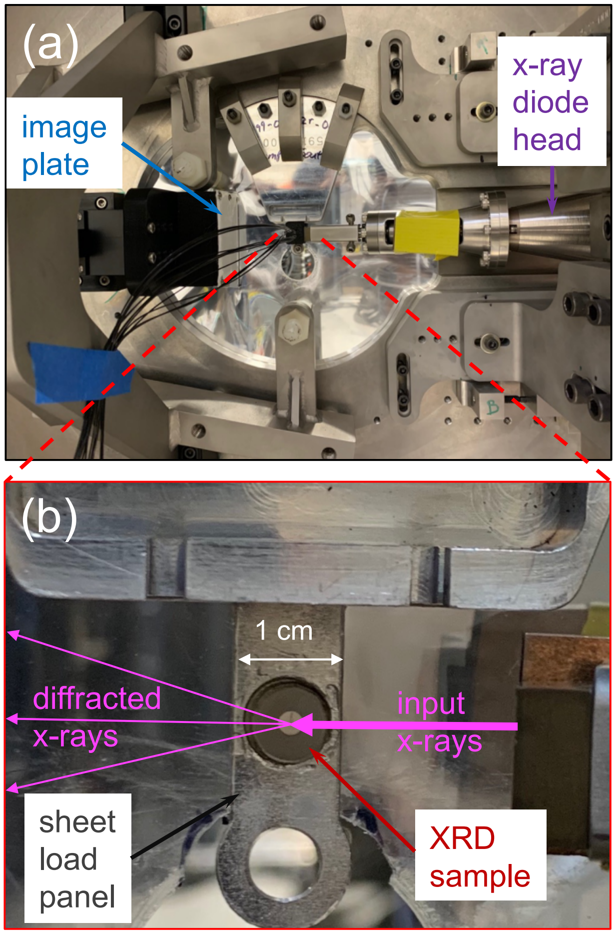

Figure 9. (a) Photo of Thor-XRD showing right-angle x-ray diode head, load panel, and image plate detector inside Thor load chamber. (b) Close-up photo of sheet load panel and XRD sample.

The typical load panel design for Thor could not be used for the XRD measurements due to the panel body pocket's side walls blocking the input and diffracted x-rays. A fast, cost-effective solution was to implement new panel design using stock 1100 Al alloy sheets cut by waterjet. Figure 9(a) presents the Thor-XRD setup showing the right-angle x-ray diode head, the “sheet load panel”, and the IP inside the expanded load chamber. Because the sheet load panels have no side walls, there is no x-ray obstruction to the input and diffracted beams, as shown in Figure 9(b).

A Fuji MS-type image plate (IP), approximately 60 mm long by 50 mm wide, was fielded inside a cassette holder that was mounted to the CPF feed plate. The IP x-ray detector was chosen for multiple reasons. First, it is a reusable and robust recording medium consisting of a highly x-ray sensitive material made from BaF(Br,I):Eu2+ phosphor crystals suspended in a plastic binder [30]. Second, the IP is capable of detecting x rays with 1–100 keV photon energies and has a dynamic range much larger than x-ray film [31, 32, 33]. Third, the IP could be quickly scanned directly to generate a digital image, without the need for chemical development. The IP was protected from the debris generated during the Thor experiment by a 1-mm thick layer of Honeywell Spectra Shield II SR-3130, made from ultra-high-molecular-weight polyethylene fiber, which is transparent to the diffracted x-rays. In addition, a thin layer of aluminized Kapton polyimide (25 μm thick) was placed in front of the IP to prevent the XRD data being erased by extraneous ultraviolet light. After the Thor-XRD experiment, the IP was recovered and scanned on a Fuji FLA-7000 IP scanner.

c. Design and modeling of experiments

The Laslo (Lagrangian Analysis and Simulation of Loading in One dimension) code [34] was used to design ramp compression experiments on Thor. Laslo is a simple transient dynamics research code that is intended to simplify the development and implementation of model equations and material models and enable rapid sensitivity and optimization studies. Laslo utilizes the same underlying mathematics and material model libraries as the 3D magnetohydrodynamics code ALEGRA [35] and has been benchmarked against it for simple 1D problems. After completion of the Thor-XRD experiment, the velocimetry measurements were compared to the Laslo simulations to determine the velocity/pressure history of the XRD sample. The process for determining the load current from velocimetry data, usually referred to as “unfolding a current” or “current unfold”, has been established and validated with material standards [36, 37]. Based on the uncertainty quantification of the current unfold method discussed by Porwitzky and Brown [38], the uncertainty of the pressures obtained from the Laslo simulations were estimated to be about a few percent.

A Thor-XRD experiment begins with designing the desired drive pulse shape. The total energy delivered to the load depends on the charge voltage of the Thor bricks. Although the capacitors within the bricks are rated at 100 kV, the peak charge voltage is usually kept below 90 kV to mitigate possible damage and increase longevity. Numerous drive pulse shapes can be generated by varying the switch firing timing of Thor's eight independent brick towers. A Thor-XRD experiment design requires calculating the arrival time of the x-rays to the XRD sample. A Laslo simulation is performed of the XRD load, which consists of the Al panel, the XRD sample, and the x-ray window. The drive pulse, current $I(t)$ or magnetic field $B(t)$, is applied to the Al panel which generates a ramp pressure wave $P(x,t)$. The ramp wave propagates from the Al panel into the XRD sample and then into the x-ray window. X-ray timing (denoted $t_{x\text{-}rays}$) is determined by when the interface between the XRD sample and x-ray window reaches the desired pressure state.

During a Thor-XRD experiment, a common trigger was sent to fire the Thor brick towers and the XRD Marx through various delay generators with the appropriate time delays. Based on the firing reproducibility tests (see Figure 5 and Figure 6(b)), the arrival of the x-rays onto the XRD sample is 100 ns after the Marx's Rogowski monitor. Prior to the downline shot, a preshot is perform by firing only the XRD Marx to obtain the sample's static XRD pattern. During the preshot, the Marx's Rogowski signal is measured and used to confirm correct firing time.

Windows are commonly used in dynamic loading experiments to allow measurement at the sample-window interface while maintaining a high-pressure state of the material close to the *in-situ* state. Two key material properties that determine window suitability for Thor-XRD experiments are shock impedance and x-ray transmission. A material's shock impedance is given by, $\rho_0 U_s$, where ρ_0 is the initial density and U_s is the shock velocity at a given particle velocity. If a window's shock impedance is much lower than the sample's shock impedance, the pressure will drop significantly as the ramp wave propagates from the sample into the window. The x-ray transmission of a material is usually characterized by its $1/e$ attenuation length or $d_{1/e}$. For example, sapphire (Al_2O_3) is a standard optical window for dynamic compression experiments, but is a poor x-ray window due to its short attenuation length (*i.e.,* $d_{1/e}$ = 0.83 mm for 17.4 keV x-rays). Alternatively, beryllium would be a good x-ray window due to its long attenuation length (*i.e.,* $d_{1/e}$ = 25.2 mm at 17.4 keV x-rays), but is not feasible for Thor-XRD experiments because Thor is not set up for contamination cleanup.

Three x-ray windows composed of polymethylpentene plastic (TPX), vitreous carbon (VC), and single-crystal lithium fluoride (LiF) were evaluated. The LiF window was oriented with the 111 reciprocal lattice vector in the direction of the pressure wave propagation, so it is denoted as LiF(111). The LiF(111) window orientation, unlike the highly inelastic LiF(100) window orientation that is typically used with velocimetry diagnostics, is known to exhibit elastic behavior up to 4 GPa [39], thereby reducing dynamic image artifacts caused by the mosaic effect. The effect due to the different orientations for the velocimetry diagnostics is minimal. The properties of these x-ray windows are listed in Table 1.

Table 1. X-ray window properties.

Window	**Ambient Density** ρ_0 **(g/cm^3)**	**Shock Velocity** U_s **(km/s)**	**Shock Impedance** $\rho_0 U_s$ **(g/cm^2/s)**	***1/e*** **attenuation length at 17.4 keV x-rays** $d_{1/e}$ **(mm)**	**Optically transparent**
TPX	0.83	2.50	2.08×10^5	25.9	Yes
VC	1.49	2.71	4.04×10^5	9.4	No
LiF(111)	2.64	5.15	1.36×10^6	3.4	Yes

Ideally, the window would be transparent to optical light and x-rays so that both velocimetry (VISAR/PDV) and XRD measurements could be simultaneously obtained. The TPX window has the lowest shock impedance and highest x-ray transmission. The LiF(111) window has the highest shock impedance and lowest x-ray transmission. Both TPX and

LiF(111) are optically transparent. The VC window has an intermediate shock impedance and intermediate x-ray transmission but is not optically transparent. It has the advantage of being amorphous, causing a minimal effect on the XRD data.

III. RESULTS AND DISCUSSION

a. Zirconium results

Zirconium (Zr) was chosen to be investigated in the initial Thor-XRD experiments. Zr is which has long been of interest to both the static [40, 41, 42] and dynamic [43, 44] high-pressure communities. At ambient pressure, Zr has a density of ρ_0 = 6.52 g/cm^3, and its structure consists of a hexagonal close-packed (hcp) α-phase ($P6_3/mmc$) lattice structure. The phase diagram by Greeff [45] estimates that under shock and ramp compression, Zr transforms to a hexagonal (hex) ω-phase (*P6/mmm*) above 3 GPa [46, 47]. At higher pressures, Zr transforms to a body centered cubic (bcc) β-phase (*Im3m*) between 24-29 GPa under shock compression [48], while it occurs above 30 GPa under ramp compression.

On Thor Expt. No. 77, the XRD load consisted of a Zr sample (0.51 mm thick, 7.9 mm diameter, 99.2% pure, temper annealed) backed by a TPX window (0.49 mm thick, 7.0 mm diameter). The Zr/TPX (sample/window) stack was glued to a sheet Al (1.11 mm thick, 10 mm wide) panel (waterjet cut) that provided the electromagnetic drive for the experiment. A LiF(100) (5.94 mm thick, 7.9 diameter) window was glued to the matching Al (1.07 mm thick, 10 mm wide) drive panel to complete the circuit. VISAR probes were fielded on both XRD and drive panels.

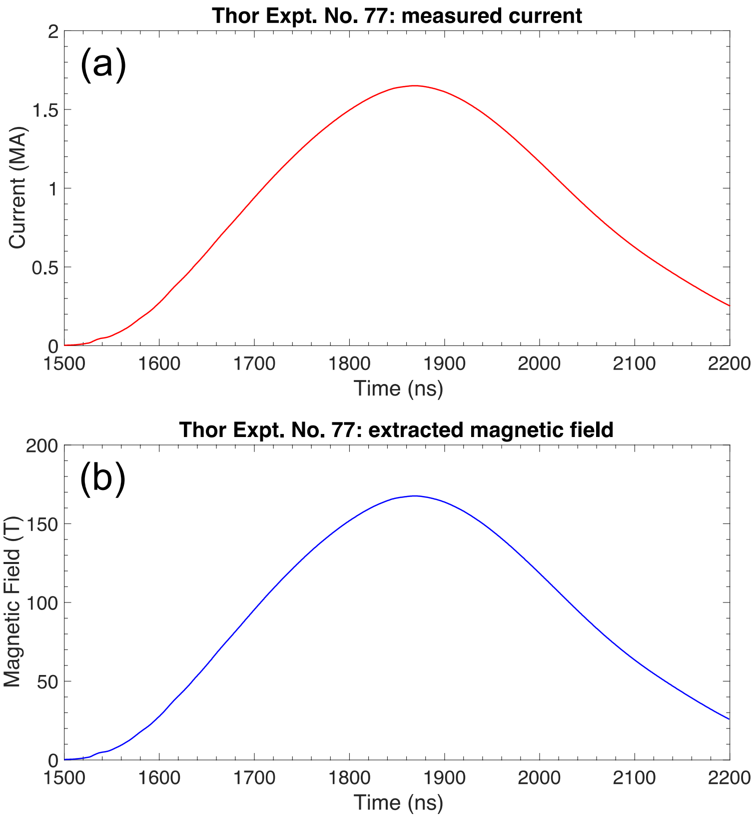

Figure 10. Thor Expt. No. 77: (a) measured current, and (b) extracted magnetic field.

Thor Expt. No. 77 went downline with a charge voltage of 90 kV, in which all of Thor’s stored energy was rapidly discharged into the load and the dynamic experiment was performed. Staggered firing of the eight groups of brick basis functions, uniformly spaced by 40 ns, produced a current pulse shape with a 265 ns risetime and a peak current of 1.65 MA, as shown in Figure 10(a). The magnetic field history may be derived by scaling the measured current by a constant factor. First, this initial magnetic field history was used in Laslo to simulate a ramp wave on the drive load to produce a velocity history at the Al/LiF(100) interface, which was then compared to the VISAR measurement. In the Laslo simulation, Sesame equation-of-state (EOS) tables [49] were used to model the Al panel (3700) [50, 51] and LiF window (7273) [52, 53]. Slight discrepancies between the Laslo and VISAR velocity histories required iterative fine-tuning of the magnetic field history until good agreement was achieved (see Figure 11(a)). Figure 10(b) shows the optimized magnetic field history that closely resembles the measured current's pulse shape and has a peak of 168 T.

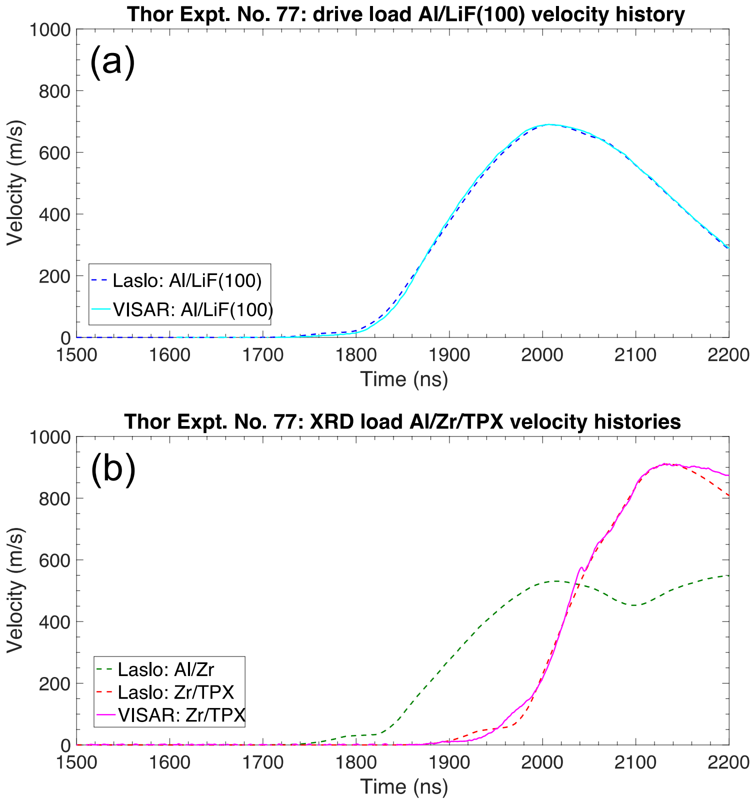

Figure 11. Thor Expt. No. 77: velocity histories from VISAR measurements and Laslo simulation at (a) drive load's Al/LiF(100) interface, and (b) XRD load's Zr/TPX interface.

Next, the optimized magnetic field history was used in Laslo to simulate a ramp wave in the XRD load. Figure 11(b) shows Laslo velocity histories at the Al/Zr interface and at the Zr/TPX interface, as well as the measured VISAR velocity history at the Zr/TPX interface. In the Laslo simulation, Sesame EOS table 3180 [49] was used for the Zr sample and a Mie-Gruneisen model was used for the TPX window. Although there were some small discrepancies between the Laslo and VISAR velocity histories at the Zr/TPX interface, general agreement was achieved.

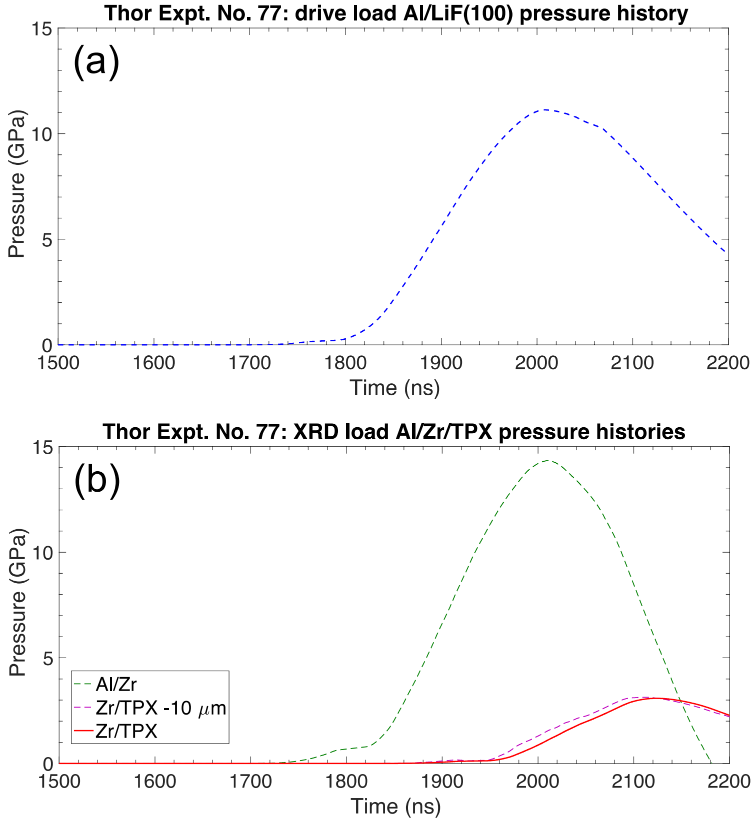

Figure 12. Thor Expt. No. 77: pressure histories from the Laslo simulation at (a) drive load's Al/LiF(100) interface, and (b) the XRD load's Al/Zr interface, Zr/TPX interface and -10 µm from it.

The Laslo simulated pressure history showed that the drive Al/LiF(100) interface reached a peak pressure of 11.13 GPa (see Figure 12(a)). Simultaneously, at the XRD load, the Al/Zr interface reached a peak pressure of 14.08 GPa due to the higher impedance of the

Zr sample (see Figure 12(b)). However, at the Zr/TPX interface the peak pressure only reached 3.08 GPa due to the much lower impedance of the TPX window. The Marx Rogowski monitor indicated the Marx firing at 2050 ns, which placed the arrival time of the x-rays to the Zr/TPX interface near peak pressure at 2150 ns (see Figure 13).

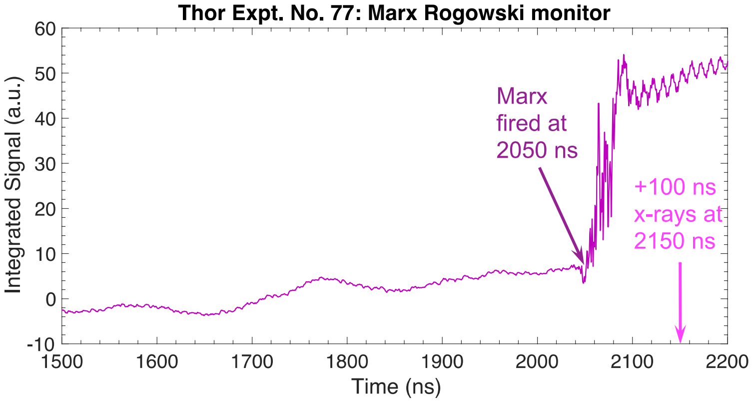

Figure 13. Thor Expt. No. 77: timing of x-rays based on the Marx Rogowski monitor's integrated signal.

Figure 14 shows the XRD patterns measured on Thor Expt. No. 77 using a Mo anode. For 17.4 keV x-rays, the Zr sample has a 1/*e* attenuation length of 98 μm. However, since the input angle is 11°, and reflected angle is also small, the penetration depth of the x-rays into the zirconium is only 10 μm, which is close to the Zr/TPX interface's pressure state (see Figure 12(b)). The preshot-static XRD pattern is shown in Figure 14(a), while the downline-dynamic XRD pattern is shown in Figure 14(b).

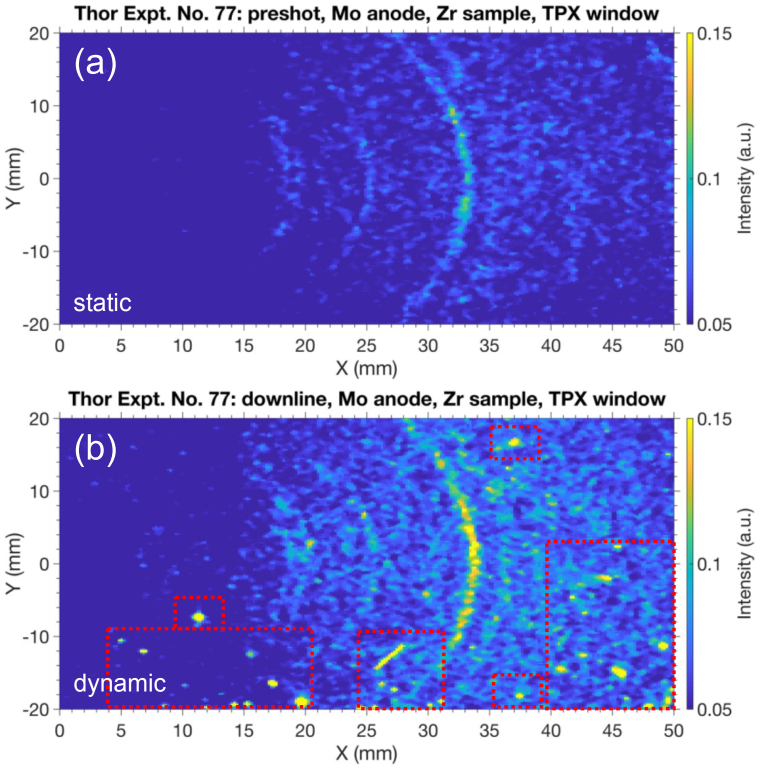

Figure 14. Thor Expt. No. 77: (a) preshot-static XRD pattern, and (b) downline-dynamic XRD pattern. The artifacts due to Thor's electrical/magnetic fringing effects are enclosed by the red dashed boxes.

The downline-dynamic XRD pattern showed an increase in the overall x-ray background and some "bright spots" which are likely electrical/magnetic artifacts from Thor fringing field on the IP x-ray detector. These artifacts were mitigated with improved electromagnetic shielding of the IP cassette holder in subsequent Thor-XRD experiments. The artifacts were masked off in the arc-integration to obtain the lineouts shown in Figure 15. The largest source of uncertainty in the angular measurement was the ability to replace the image plate from its static-preshot position to the dynamic-downline position. A series of ambient XRD shots were performed for a fixed XRD setup by switching out and processing the multiple image plates. The statistical distribution of those angular measurements determined the angular uncertainty.

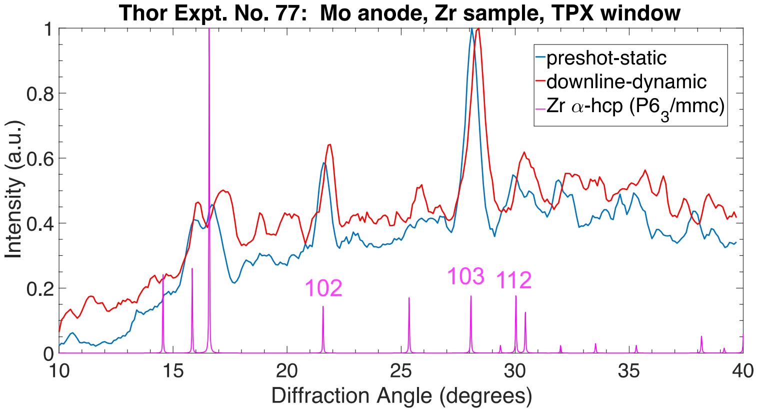

Figure 15. Thor Expt. No. 77: arc-integrated lineouts of the preshot-static XRD, and the downline-dynamic XRD, and the Zr α-hcp (*P6$_3$/mmc*) structure's XRD peaks.

The preshot-static lineout agrees well with multiple peaks of the Zr α-hcp (*P6$_3$/mmc*) structure. The downline-dynamic lineout looked similar except the diffraction peaks were shifted to higher diffraction angles. The total shift in the diffraction peaks is the result of two effects: (1) the lattice compression of the Zr sample, and (2) the offset distance between the preshot and downline XRD patterns caused by the Zr/TPX interface motion. According to the Laslo simulation, the Zr/TPX interface had moved 100 μm when the x-rays arrived at $t_{x\text{-}rays}$ = 2150 ns. After accounting for the Zr/TPX interface motion's translational offset, the three strongest diffraction peaks (*i.e., hkl* = 102, 103, 112) had shifts *(i.e., $\Delta\theta$* = 0.22°, 0.27°, 0.38° ± 0.10°) that corresponded to a lattice compression of the Zr sample of $\Delta d/d$ = 0.010 ± 0.001 which agreed within uncertainty with the Laslo simulation of 3.08 GPa.

b. Aluminum results

The purpose of the next set of Thor-XRD experiments was to confirm the x-ray timing along the ramp wave compression profile and to examine effects of the x-ray window on the dynamic XRD patterns. In these experiments, the Al panel itself was the XRD sample. Aluminum at ambient conditions has the face-centered cubic (fcc) structure ($Fm\overline{3}m$) and a density of 2.70 g/cm^3. On Thor Expt. No. 127, the XRD load consisted of a LiF(111) window (0.38 mm thick, 16.0 mm diameter) glued to an Al sheet panel (1.04 mm thick, 10 mm wide) that provided the electromagnetic drive for the experiment. A LiF(100) window (5.98 mm thick, 7.9 diameter) was glued to the matching drive load Al panel (1.07 mm thick, 10 mm wide). VISAR/PDV probes were fielded on both XRD and drive panels. For 17.4 keV x-rays, the Al sample has a 1/*e* attenuation length of 770 μm. With an input angle of 11º, this corresponds to a nominal penetration depth of 75 μm.

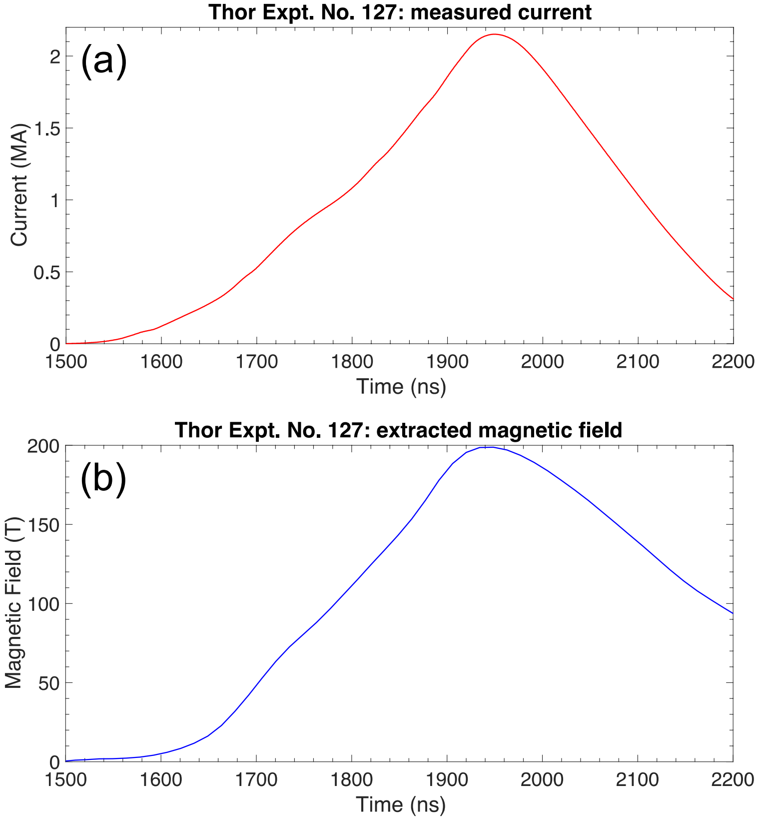

Figure 16. Thor Expt. No. 127: (a) measured current, and (b) extracted magnetic field.

Thor Expt. No. 127 went downline with a charge voltage of 90 kV. Staggered firing of the eight groups of brick towers with a nonuniform time-spacing produced a current pulse shape with a 270 ns risetime and a peak current of 2.1 MA (see Figure 16(a)). A magnetic field history was derived by scaling the measured current and optimization, which produced a similar pulse shape with a peak magnetic field of 198 T, as shown in Figure 16(b). The optimized magnetic field history was used in Laslo to simulate ramp waves on both the drive and XRD loads.

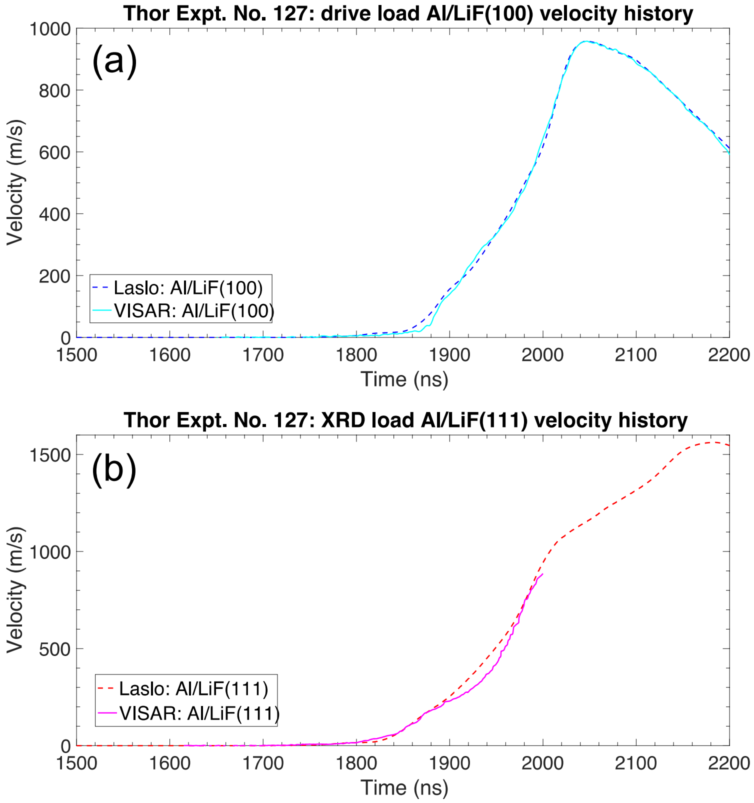

Figure 17. Thor Expt. No. 127: velocity histories from VISAR measurements and Laslo simulation at (a) drive load's Al/LiF(100) interface, and (b) XRD load's Al/LiF(111) interface.

Although slight discrepancies between the Laslo and VISAR velocity histories at the drive load's Al/LiF(100) interface were observed, the overall agreement was acceptable (see Figure 17(a)). Figure 17(b) shows that the Laslo and VISAR velocity histories at the XRD load's Al/LiF(111) interface agreed reasonably well until the LiF(111) window's free surface moved significantly (at ~ 2000 ns), disrupting the VISAR measurement.

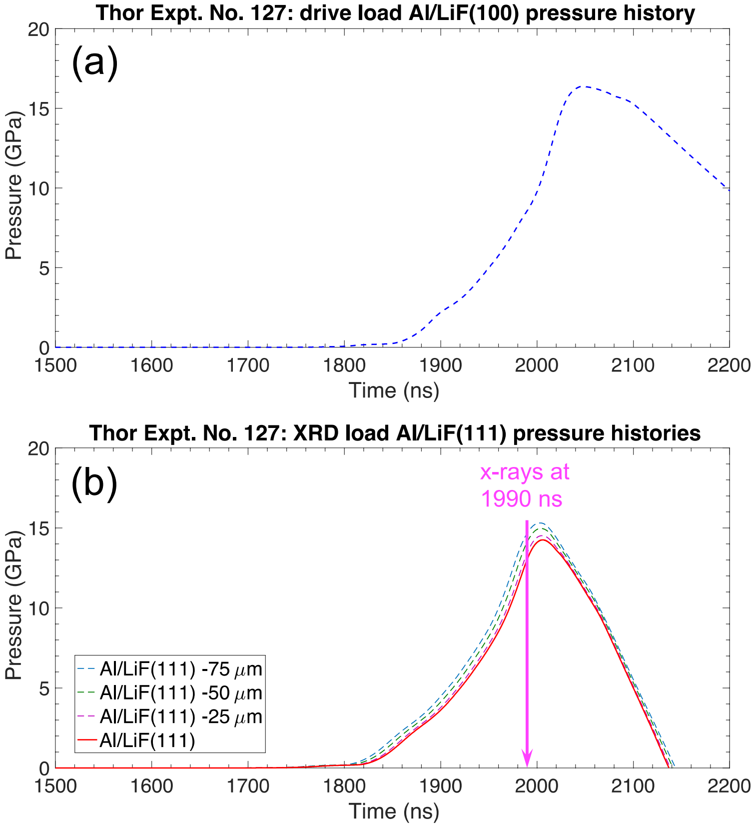

Figure 18. Thor Expt. No. 127: pressure histories from the Laslo simulation at (a) drive load's Al/LiF(100) interface, and (b) the XRD load's Al/LiF(111) interface, and -25, -50, and -75 μm away from it.

The Laslo simulated pressure history showed that the drive load's Al/LiF(100) interface reached a peak pressure of 16.51 GPa (see Figure 18(a)). At the XRD load, the foot of the ramp wave reaches the thin LiF(111) window's free surface around 1900 ns, which initiated a release wave moving back to Al/LiF(111) interface, thus it only reached a peak pressure of 13.64 GPa (see Figure 18(b)). The Marx Rogowski monitor showed the Marx firing at 1890 ns, placing the x-ray arrival time at the Al/LiF(111) interface at 1990 ns, near peak pressure. A histogram of the Laslo simulated pressure states of the Al compressed sample that included the x-rays' pulse length (30 ns) and penetration depth (75 um) showed the distribution pressure states probed by the XRD measurement, which were within 7% of the Al/LiF(111) interface's pressure (see Figure 19).

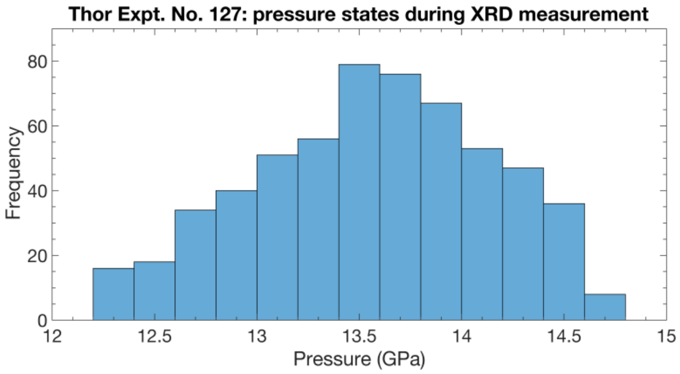

Figure 19. Thor Expt. No. 127: histogram of pressure states during XRD measurement.

Figure 20 shows the XRD patterns measured on Thor Expt. No. 127. The preshot-static XRD pattern is shown in Figure 20(a), while the downline-dynamic XRD pattern is shown in Figure 20(b). On the preshot-static XRD pattern, the bright LiF(111) Laue spots are round and oval. However, on the downline-dynamic XRD pattern, the LiF(111) Laue spots were distorted and elongated as the LiF(111) window underwent compression. The LiF(111) Laue spots were masked off in the arc-integration to obtain the lineouts shown in Figure 21. For the aluminum experiment, no filter was used, so the weak K-β line emission shown in Figure 4 produced additional diffraction lines to the main ones produced by the K-α line emission. The K-β (311) reflection was observed at around 30° and the K-β (220) reflection was observed at around 25°. The other K-β reflections were obscured by the dominant K-α line reflections.

The preshot-static lineout shows the multiple peaks of the Al fcc ($Fm\overline{3}m$) structure. The downline-dynamic lineout looked similar except its diffraction peaks were clearly shifted to higher diffraction angles. At the x-ray arrival time of $t_{x\text{-}rays}$ = 1990 ns, the Al/LiF(111) interface only moved 60 μm due to the magnitude of the drive, and the EOS/shock impedances of the Al panel and LiF(111) window. Looking at the three strongest diffraction peaks (*i.e., hkl* = 200, 220, 311), the shifts (*i.e.,* $\Delta\theta$ = 1.28°, 1.72°, 2.12° ± 0.10°) corresponded to a lattice compression of the Al sample of $\Delta d/d = 0.061 \pm 0.006$, which was close to the Laslo simulation pressure of 13.64 GPa.

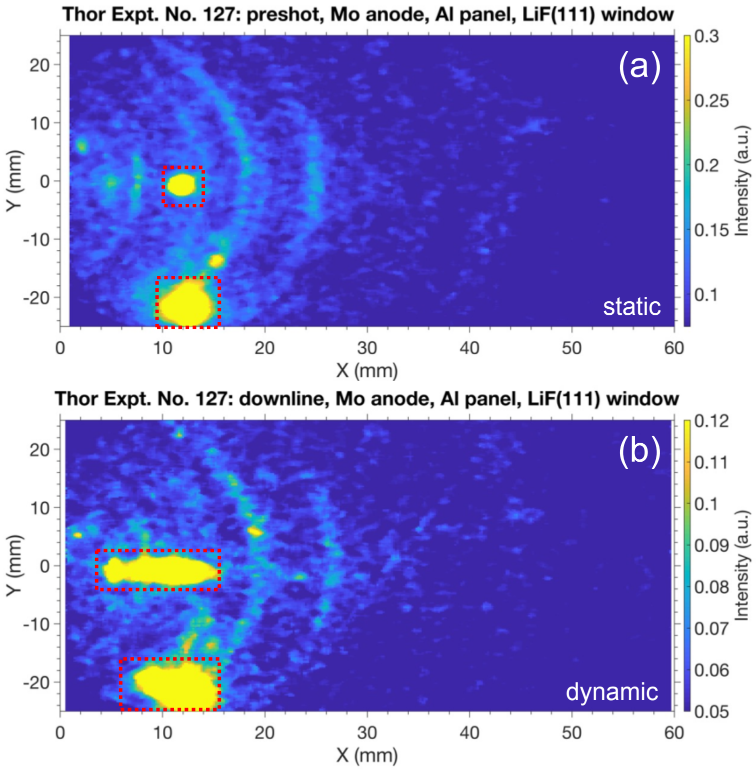

Figure 20. Thor Expt. No. 127: (a) preshot-static XRD pattern, and (b) downline-dynamic XRD pattern. The LiF(111) Laue spots are enclosed by the red dashed boxes.

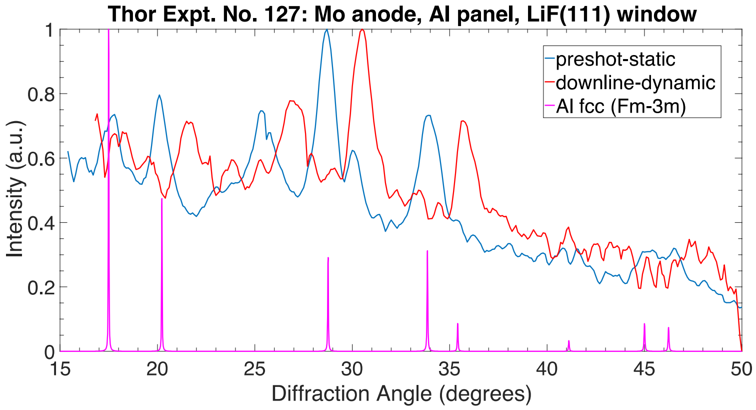

Figure 21. Thor Expt. No. 127: arc-integrated lineouts of the preshot-static XRD, and the downline-dynamic XRD, and the Al fcc ($Fm\bar{3}m$) structure's XRD peaks.

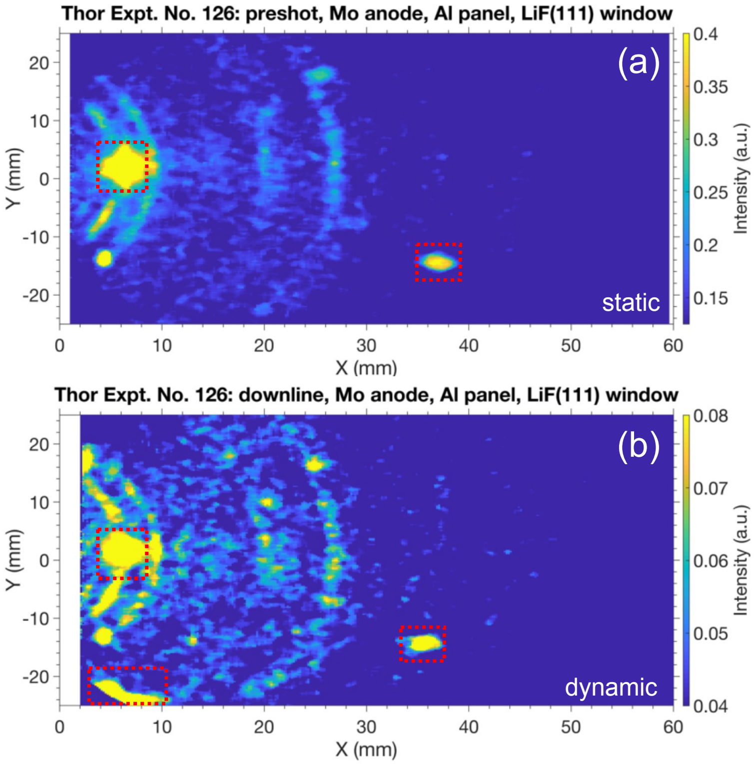

Figure 22. Thor Expt. No. 126: (a) preshot-static XRD pattern, and (b) downline-dynamic XRD pattern. The LiF(111) Laue spots are enclosed by the red dashed boxes.

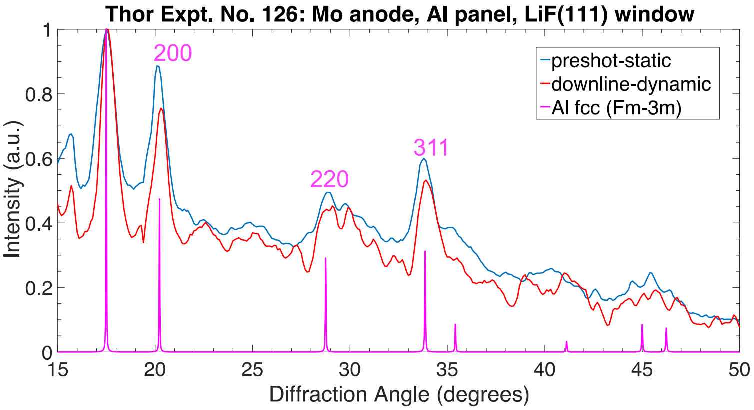

Figure 23. Thor Expt. No. 126: arc-integrated lineouts of the preshot-static XRD, the downline-dynamic XRD, and the Al fcc ($Fm\bar{3}m$) structure's XRD peaks.

Other Thor-XRD experiments were performed with the same load parameters (*i.e.,* Al panel with LiF(111) window) and drive pulse, but at varying x-ray timings. For example, Thor Expt. No. 126 had an x-ray arrival time of 1840 ns, which corresponded to a very small 3 µm motion of the Al/LiF(111) interface. In this case, only a very small change in the downline-dynamic XRD pattern was seen compared to the preshot-static XRD pattern (see Figure 22), and on order of 0.1° of shift was observed (see Figure 23). This corresponds to an Al sample lattice compression of $\Delta d/d = 0.0010 \pm 0.0005$ and a pressure of 0.54 GPa.

Alternatively, Thor Expt. No. 138 had an x-ray arrival time of 1950 ns, which was later than Thor Expt. No. 126 but earlier that Thor Expt. No. 127 and corresponded to a slight

20 μm motion of the Al/LiF(111) interface. As expected, the downline-dynamic XRD pattern was clearly shifted from its preshot-static XRD pattern (see Figure 24), but the LiF(111) Laue spots were only moderately deformed. Figure 25 shows arc-integrated lineouts for the preshot and downline XRD patterns. The resulting shifts ($\Delta\theta$ = 0.34°, 0.45°, 0.52° ± 0.10°) corresponded to an Al lattice compression of $\Delta d/d = 0.031 \pm 0.003$, which was close to the Laslo simulation pressure of 7.59 GPa.

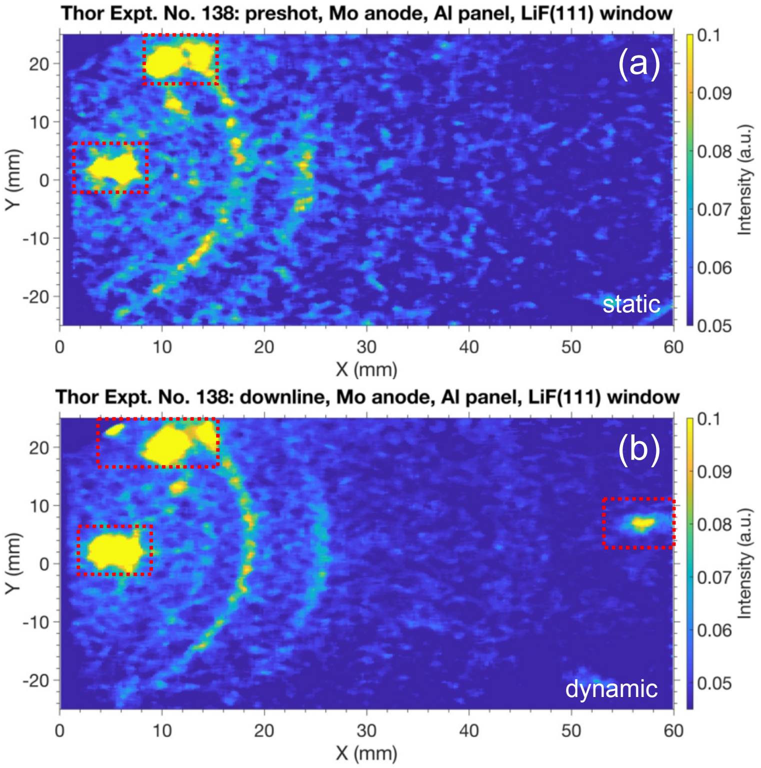

Figure 24. Thor Expt. No. 138: (a) preshot-static XRD pattern, and (b) downline-dynamic XRD pattern. The LiF(111) Laue spots are enclosed by the red dashed boxes.

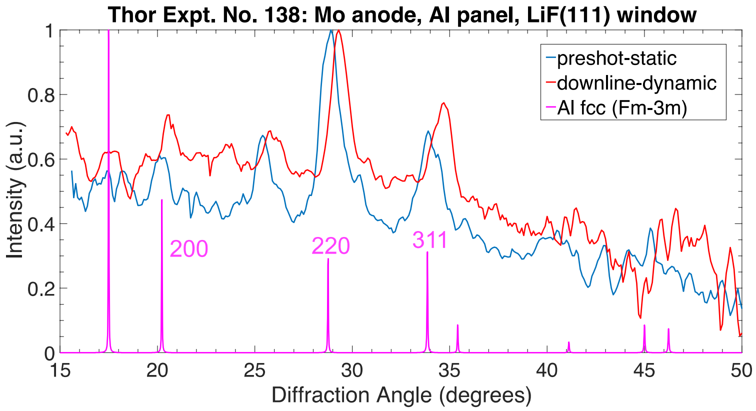

Figure 25. Thor Expt. No. 138: arc-integrated lineouts of the preshot-static XRD, the downline-dynamic XRD, and the Al fcc ($Fm\overline{3}m$) structure's XRD peaks.

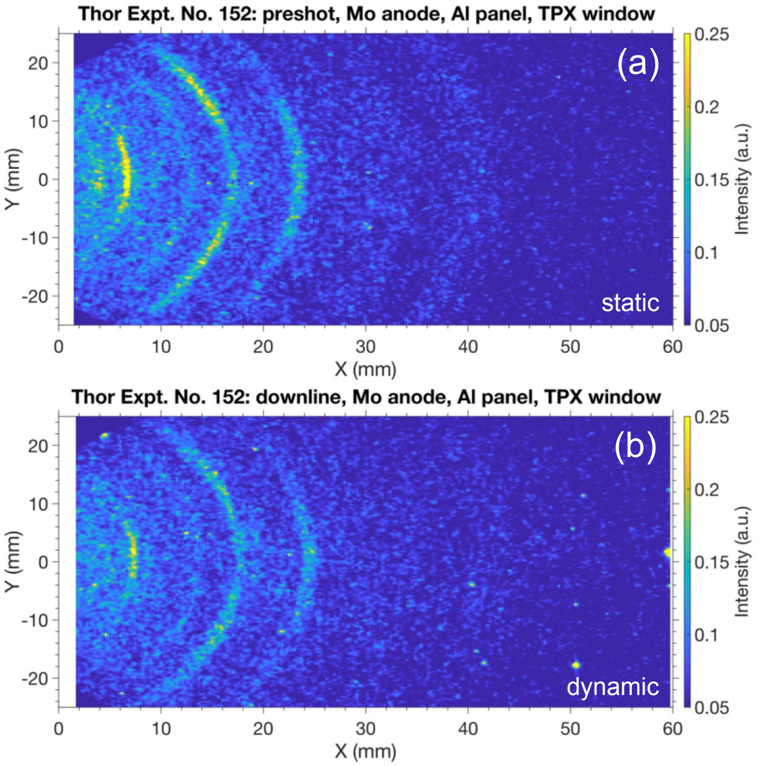

Figure 26. Thor Expt. No. 152: (a) preshot-static XRD pattern, and (b) downline-dynamic XRD pattern.

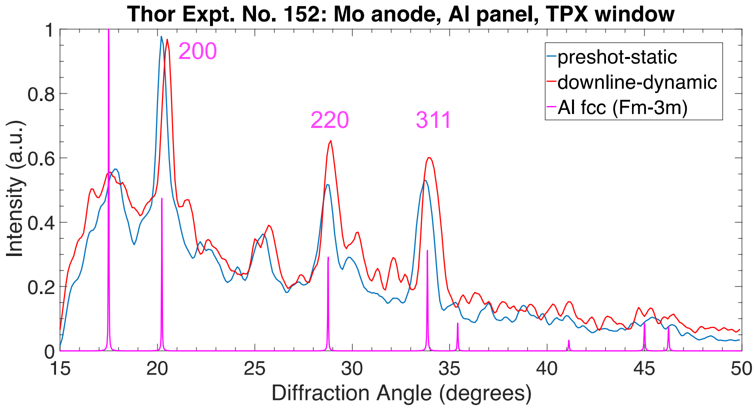

Figure 27. Thor Expt. No. 152: arc-integrated lineouts of the preshot-static XRD, the downline-dynamic XRD, and the Al fcc ($Fm\bar{3}m$) structure's XRD peaks.

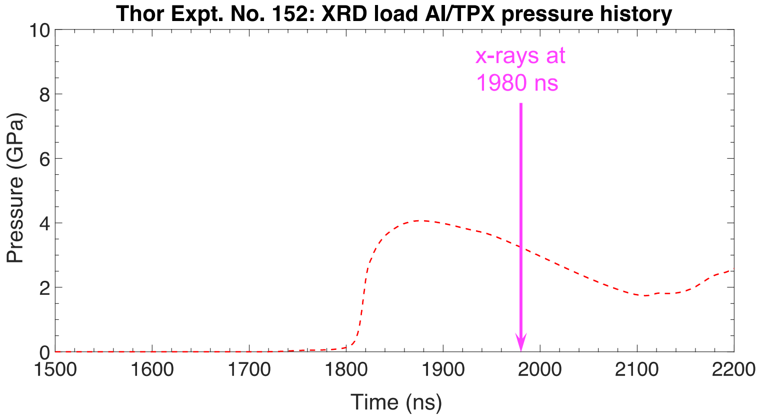

Figure 28. Thor Expt. No. 152: pressure history from the Laslo simulation at the XRD load's Al/TPX interface.

To examine the effect that different x-ray windows have on the quality of the Thor-XRD measurement, a TPX window (2 mm thick) was utilized instead of the LiF(111) window on Thor Expt. No. 152. Figure 26 shows that both preshot-static and downline-dynamic XRD patterns were much clearer with the TPX window. Without the need to mask off any window artifacts, the arc-integrated lineouts were obviously improved (see Figure 27). However, due to the TPX's lower impedance, the Al/TPX interface had moved 180 μm at $t_{x\text{-}rays}$ = 1980 ns, with a much lower pressure of 3.25 GPa (see Figure 28). Accounting for the large translational offset, the resulting shifts (*i.e.,* $\Delta\theta$ = 0.12°, 0.08°, 0.15° ± 0.10°) corresponded to an Al lattice compression of $\Delta d/d = 0.009 \pm 0.001$. The results of the Al compression Thor-XRD experiments are summarized in Figure 29. For each experiment, the compressed Al density is inferred from the XRD measured lattice compression and compared to the corresponding Laslo simulation's density in Table 2. In summary, the timing of the x-rays relative to the drive pulse was determined using the Al compression experiments. Thor Expt. Nos. 126, 138, 152, and 127, which measured shifts in the Al XRD peaks at various time points ($t_{x\text{-}rays}$ = 1840, 1950, 1980 and1990 ns, respectively), corresponded well with the ramp profile that was measured by velocimetry and predicted by the Laslo simulations. At the earliest time, Thor Expt. No. 126 showed very small but still measurable shifts in the Al XRD peaks, which indicated the ramp wave has just reached the Al/LiF interface when the x-rays arrived. Based on these results, and the x-ray pulse length (30 ns) and jitter (5 ns), we estimate the uncertainty in the x-ray timing to be approximately 50 ns. Additional Al compression experiments at smaller time steps would be needed to reduce the timing uncertainty.

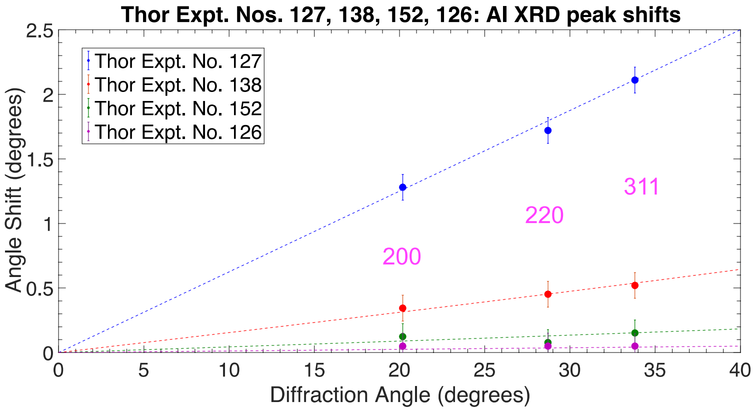

Figure 29. Thor Expt. Nos. 127, 138, 152, and 126: Al lattice compressions from the shifts of Al fcc XRD peaks (*hkl* = 200, 220, 311).

Table 2. Comparison of compressed Al densities from XRD measured lattice compression and Laslo simulation using Sesame EOS 3700.

Thor Expt. No.	**XRD Measurement**		**Laslo Simulation**	
	Lattice Compression	**Inferred Density (g/cm^3)**	**Sesame EOS 3700 Density (g/cm^3)**	**Sesame EOS 3700 Pressure (GPa)**
127	0.061 ± 0.006	3.225 ± 0.055	3.076	13.64
138	0.031 ± 0.003	2.959 ± 0.026	2.932	7.59
152	0.009 ± 0.001	2.774 ± 0.008	2.805	3.25
126	0.0010 ± 0.0005	2.708 ± 0.004	2.725	0.54

c. Single-crystal cadmium sulfide results

The objective of the next set of Thor-XRD experiment was to measure a phase change of a material under ramp compression. Cadmium sulfide (CdS) is a yellow solid that occurs in two crystal forms under ambient conditions: (1) the more stable wurtzite-hexagonal structure ($P6_3mc$), and (2) the less common zincblende-cubic structure ($F\bar{4}3m$). Cadmium sulfide exhibits a diffusionless structural transformation (*i.e.,* military or Martensitic) from 4-neighbor coordinated wurtzite-hex to 6-neighbor coordinated rocksalt-fcc ($Fm\bar{3}m$) structure between 3 and 9 GPa.

Knudson *et al.* [54, 55] used shock loading to show that the nature and time scale of this transition depends on the crystal orientation (*i.e.*, along the a-axis or c-axis) and the peak loading pressure. They determined that at pressures just above the quasistatically observed transition pressure, shock loaded CdS required relatively long (> 10 ns) incubation times before transition, while at higher pressures the transition was nearly instantaneous. Moreover, this kinetics-driven incubation time depended on orientation, such that the incubation time decreased abruptly to zero time above a critical pressure in the c-axis loaded cases, while for the a-axis loaded cases the incubation time deceased smoothly with pressure [56]. In the a-axis orientation, evidence was found for inelastic deformation before the onset of the phase transition, which may influence the mechanism.

A phase transformation kinetics model [57] was developed for CdS. This model requires an independent EOS for each phase of interest along with the empirical transformation rate parameters. The wurtzite and rocksalt phases were both modeled with a Vinet room temperature isotherm reference curve coupled to a Mie-Gruneisen thermal approximation to complete the equation of state; the parameters are given in Table 3.

Table 3. Parameter for Vinet models of CdS.

Phase	**Ambient Density ρ_0 (g/cm^3)**	**Ambient Bulk Modulus B_0 (GPa)**	**Pressure Derivative of Bulk Modulus B_0'**	**Thermal Expansion α (1/°C)**	**Specific Heat c_v (J/g°C)**
Wurtzite	4.828	93.94	1.0	1.41e-5	0.33
Rocksalt	5.914	78.49	4.07	2.97e-5	0.33

For wurtzite, the initial density, ρ_0, ambient bulk modulus, B_0, and the pressure derivative of the bulk modulus, B_0', were fit to the elastic fit from Tang and Gupta [58]. The thermal expansion, α, and specific heat, c_v, are assumed to remain constant within the EOS approximation so their ambient values are used. The rocksalt phase Vinet reference curve parameters were determined through a fit to the DAC data of Li *et al.* [59]. Li *et al.* also reported a value for the thermal expansion coefficient, while density functional theory (DFT) calculations suggest there is not a significant change in the specific heat across the phases [60]. Finally, an energy offset is applied to the rocksalt phase to shift the relative energies to obtain an equilibrium phase transition pressure along the 300 K isotherm of 2.6 GPa [59]. The phase transition kinetic parameters were determined by empirical tuning to obtain a best fit to the measured Thor data where fit values of $\beta = 6 \times 10^4$ J/kg and $\eta = 1 \times 10^5$ s^{-1} were obtained. However, this kinetic model results in significant metastability such that the observed transition pressure is ~ 6 GPa, well beyond the estimated equilibrium point of 2.6 GPa.

Single-crystal (wurtzite) c-axis CdS samples were obtained from SurfaceNet GmbH for the Thor-XRD experiments. The c-axis CdS sample had the (001) axis perpendicular to its flat surfaces and the location of an a-axis (110) marked on its edge. On Thor Expt. No. 154, the XRD load consisted of a c-axis CdS sample (0.51 mm thick, 7.9 mm diameter), backed by a VC window (0.42 mm thick, 16 mm diameter). The sample/window stack was glued to an Al sheet panel (1.07 mm thick, 10 mm wide) that provided the electromagnetic drive for the experiment. A LiF(100) window (5.96 mm thick, 7.9 diameter) was glued to the matching Al drive panel (1.13 mm thick, 10 mm wide). VISAR/PDV probes were fielded on both the XRD and drive panels. For 17.4 keV x-rays, the CdS sample has a 1/*e* attenuation length of 90 μm, if extinction effects are disregarded. With an input angle of 11º, this corresponds to a nominal penetration depth of 9 μm to the CdS sample.

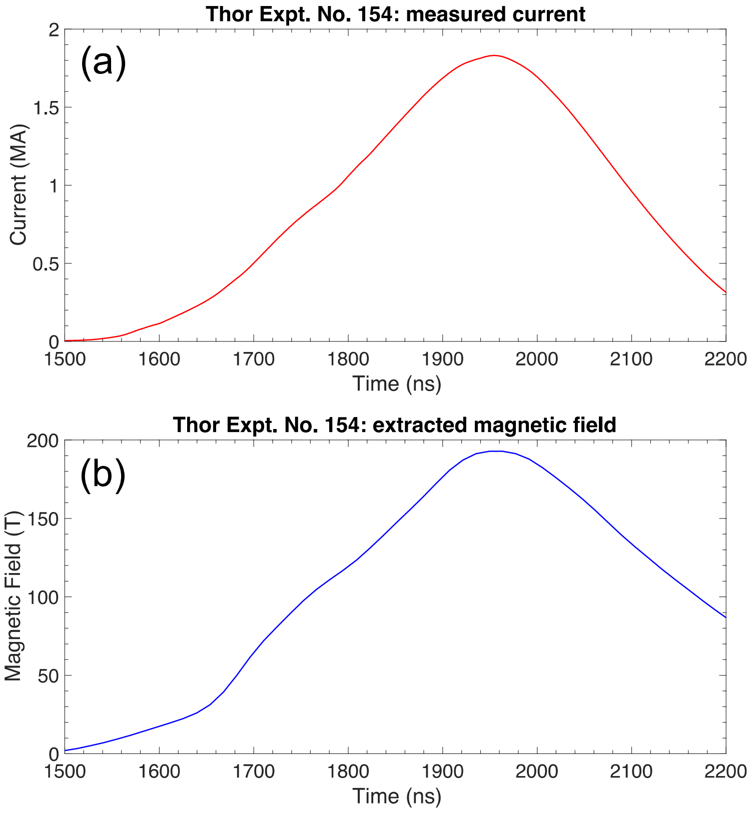

Figure 30. Thor Expt. No. 154: (a) measured current, and (b) extracted magnetic field.

Thor Expt. No. 154 went downline with a charge voltage of 90 kV. Staggered firing of the eight groups of brick towers with a nonuniform time-spacing produced a current pulse shape with a 270 ns risetime and a peak current of 1.85 MA (see Figure 30(a)). A magnetic field history was derived by scaling the measured current and optimization, which produced a similar pulse shape with a peak magnetic field of 193 T, as shown in Figure 30(b).

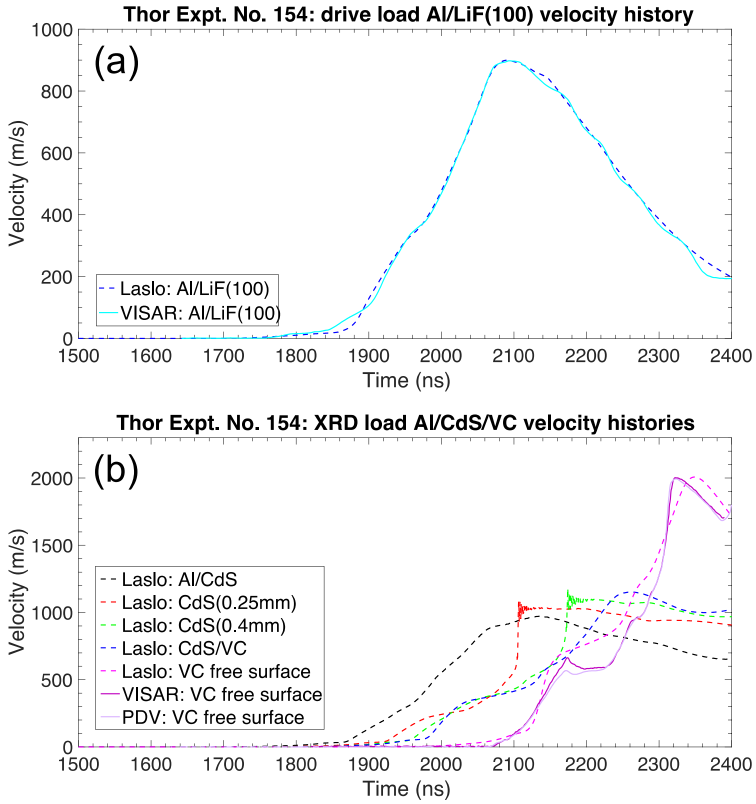

Figure 31. Thor Expt. No. 154: velocity histories from VISAR/PDV measurements and Laslo simulation at (a) drive load's Al/LiF(100) interface, and (b) XRD load's Al/CdS interface, CdS (0.25 mm), CdS (0.4 mm), CdS/VC interface, and VC free surface.

The optimized magnetic field history was used in a Laslo simulation to simulate a ramp wave into a CdS sample that was described by the phase transformation kinetics model [57], which was backed by a VC window that was described by a Mie-Gruneisen model. Looking at the drive load, Figure 31(a) shows general agreement between the Laslo simulation and the measured Al/LiF(100) velocity history. On the XRD load, Figure 31(b) shows the Laslo simulated velocity histories at the Lagrangian positions: Al/CdS interface, CdS (0.25mm), CdS (0.4 mm), CdS/VC interface and -9 µm from it. In addition, the Laslo simulated VC free surface velocity history is compared with the VISAR/PDV measured velocity histories.

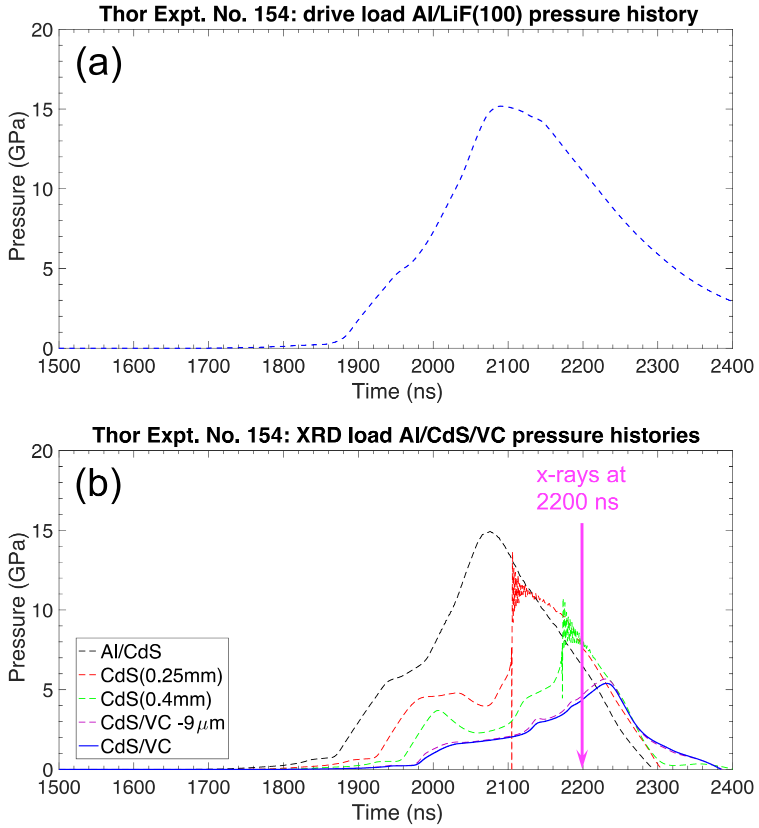

Figure 32. Thor Expt. No. 154: pressure histories from the Laslo simulation at (a) drive load's Al/LiF(100) interface, and (b) the XRD load's Al/CdS interface, CdS (0.25 mm), CdS (0.4 mm), CdS/VC interface and -9 μm from it.

Figure 32(a) shows that the drive Al/LiF(100) interface reached a peak pressure of 15.18 GPa. The Laslo simulated pressure histories at the Al/CdS interface, CdS (0.25 mm), CdS (0.4 mm), and CdS/VC interface are shown in Figure 32(b). As the ramp wave propagates into the CdS sample, the wurtzite-to-rocksalt phase change caused a definitive steepening to occur. At the CdS/VC interface, the effect is less noticeable but still indicative of the phase change.

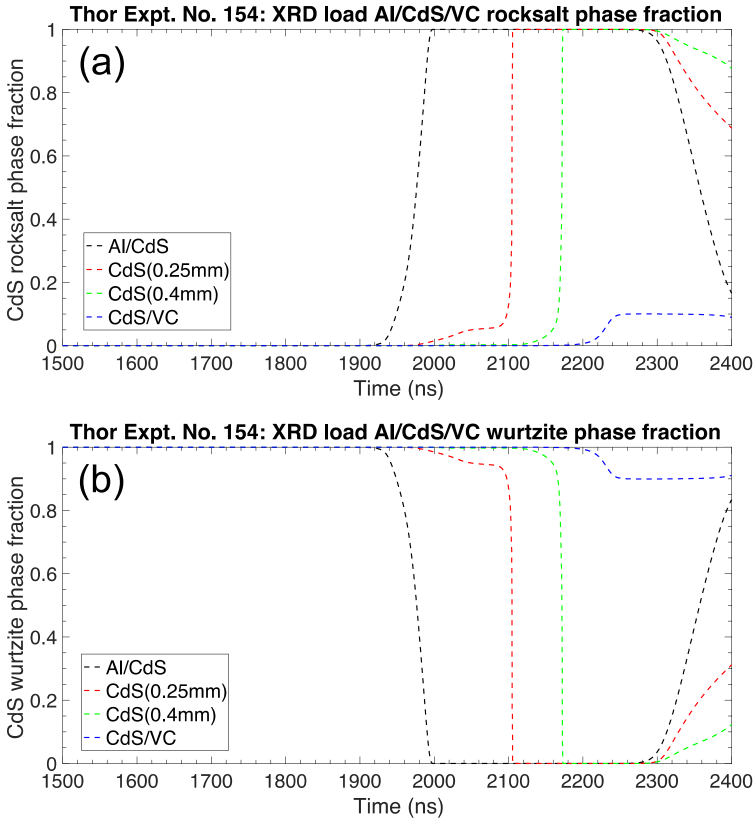

Figure 33. Thor Expt. No. 154: phase fractions from the Laslo simulation at Al/CdS interface, CdS (0.25 mm), CdS (0.4 mm), CdS/VC interface of (a) wurtzite, and (b) rocksalt.

Figure 33 shows the Laslo simulated phase fractions of the CdS wurtzite and rocksalt phases. Interestingly, the phase transformation kinetics model predicts within the CdS sample (*e.g.,* at 0.25 and 0.4 mm) a full phase change occurs, but near the CdS/VC interface only a partial phase change occurs leaving this region of the CdS sample in a mixed-phase state. The arrival time of the x-rays on the CdS/VC interface was 2200 ns.

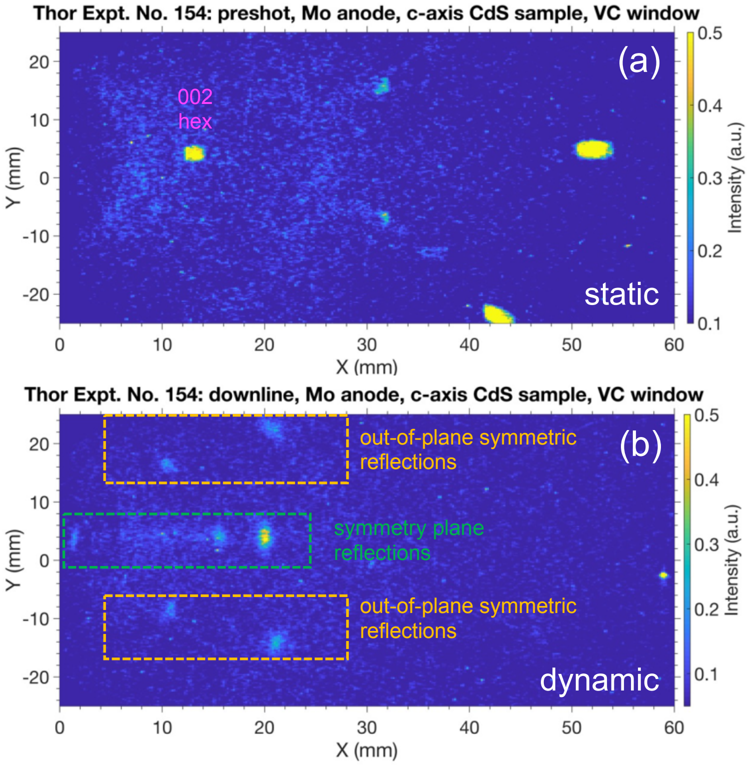

Figure 34. Thor Expt. No. 154: (a) preshot-static XRD pattern, and (b) downline-dynamic XRD pattern.

Figure 34 shows the XRD patterns measured on Thor Expt. No. 154. The preshot-static XRD pattern is shown in Figure 34(a), and the downline-dynamic XRD pattern is shown in Figure 34(b). The c-axis CdS sample was oriented such that the a-axis was perpendicular to the input x-ray beam. The preshot-static XRD pattern's Laue spots are consistent with the CdS wurtzite-hexagonal structure. The downline-dynamic XRD pattern clearly shows a new set of spots, which consisted of multiple regions of interest. Specifically, the spots along the central axis are from "symmetry plane reflections" and the off-axis spots are from “out-of-plane reflections” (see Figure 34(b)). The original 002 hex CdS Laue bremsstrahlung reflection in the preshot-static symmetry plane (see Figure 34(a)) is observed to blur over a significant range of scattering angles, indicating that the single crystal has transformed into a highly oriented, mosaic powder. This hypothesis is further supported by the observation that the new spots are elongated in the direction of the Debye-Scherrer rings, and that the other preshot-static Laue spots at high scattering angles are no longer observed.

The hypothesis that the new spots are Debye-Scherrer rings allows arc-integration for phase identification, because some newly formed domains rotate into angles that satisfy the Bragg condition for the 17.4 keV Mo anode x-ray source characteristic line, filtered with a 25 μm Zr filter at the slit collimator. Figure 35(a) shows the arc-integrated lineouts for the symmetry plane where the 002 fcc and 004 fcc and 004 hex lines are identified. First, the 004 hex reflection observed at 26.1° indicates remnants of the wurtzite-hex structure. Second, the 002 fcc and 004 fcc reflections observed at 14.5° and 29.7°, respectively, show the formation of new material with the rocksalt-fcc structure. The abrupt cutoff of the streak of reflected continuum x-rays at the diffraction angle of 18º is interpreted as reflections at x-ray energies near the 26.7 keV cadmium K-edge from the new 004 fcc phase.

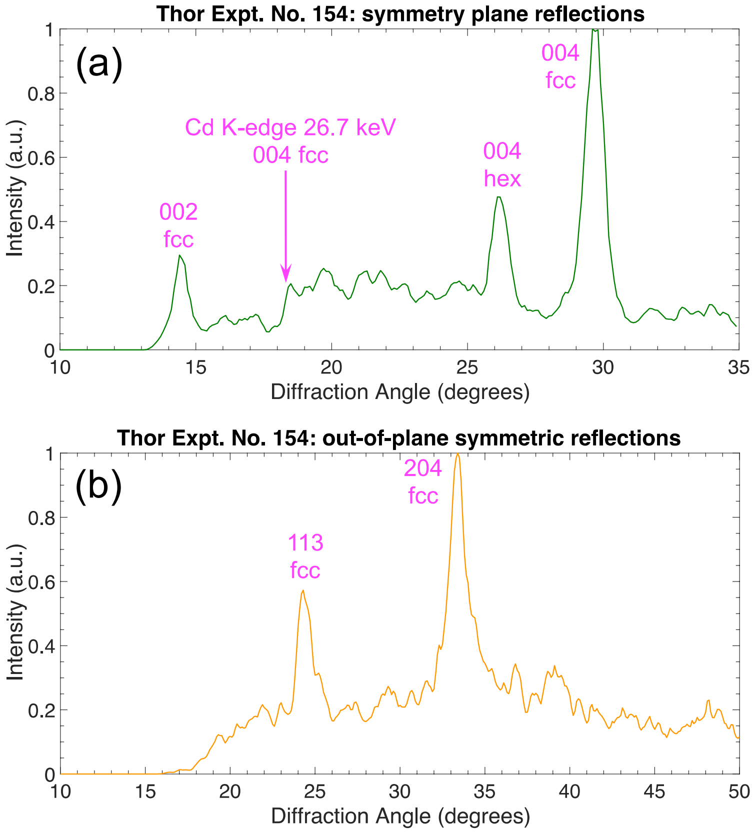

Figure 35. Thor Expt. No. 154: (a) arc-integrated lineouts of symmetry plane reflections, and (b) arc-integrated lineouts of out-of-plane symmetric reflections.

Debye-Scherer ring integration was also performed on the symmetric out-of-plane reflections (see Figure 35(b)). The scattering angles were observed to be consistent with rocksalt 113 fcc and 204 fcc reflections at 17.4 keV. The only observed reflections for both the hex and fcc phases have *hkl* indices with *l* large compared with *h* and *k*. Other reflections are out of the field-of-view of the IP detector.

Figure 36 and Figure 37 shows how the scattering angles and spot locations for the rocksalt-fcc lattice orientation were determined with 3-dimensional ray tracing. Three distinct orientations were predicted for the rocksalt-fcc phase with respect to the original CdS wurtzite-hexagonal phase, as shown in Figure 37. In this schematic, the three orientations are labelled “A”, “B”, and “C”. In Figure 36, the 113 fcc reflections are consistent with the “B” orientation, however, the 204 fcc reflections in this orientation are out of the field-of-view (see Figure 36). Whereas the observed 113 fcc spots are caused by the “B” orientation, the 204 fcc reflections are explained as one reflection each from the “A” and “C” orientations. Therefore, the 30° 12-fold symmetry of the domains in the new rocksalt-fcc structure phase is required to explain the experimental observations. Thus, the identification of the ramp-pressure-induced phase transformation in CdS clearly indicates importance of XRD on pulsed-power platforms. This new XRD diagnostic will dramatically improve our predictive capability and understanding of rate-dependent behavior at or near phase transitions.

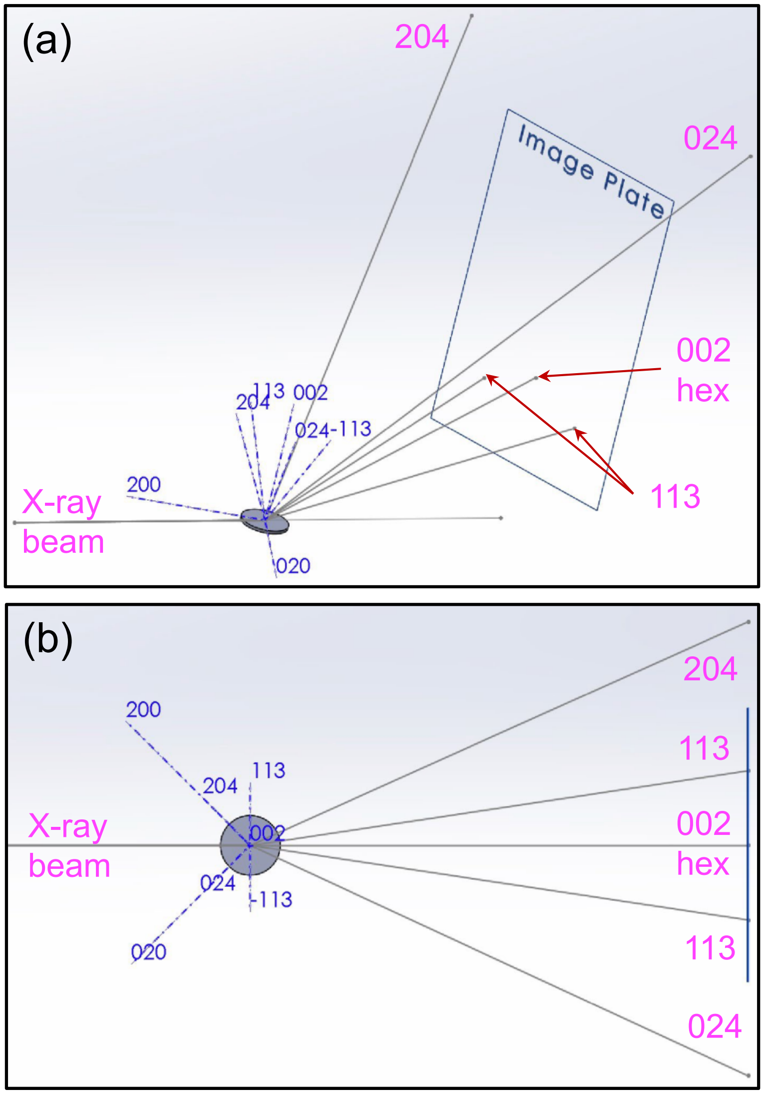

Figure 36. Thor Expt. No. 154: explanation for dynamic 113 fcc spots in the out-of-plane symmetric reflections through (a) the isometric view, and (b) the view along the c-axis. The 002 hex reflection indicates the position of the preshot-static Laue spot.

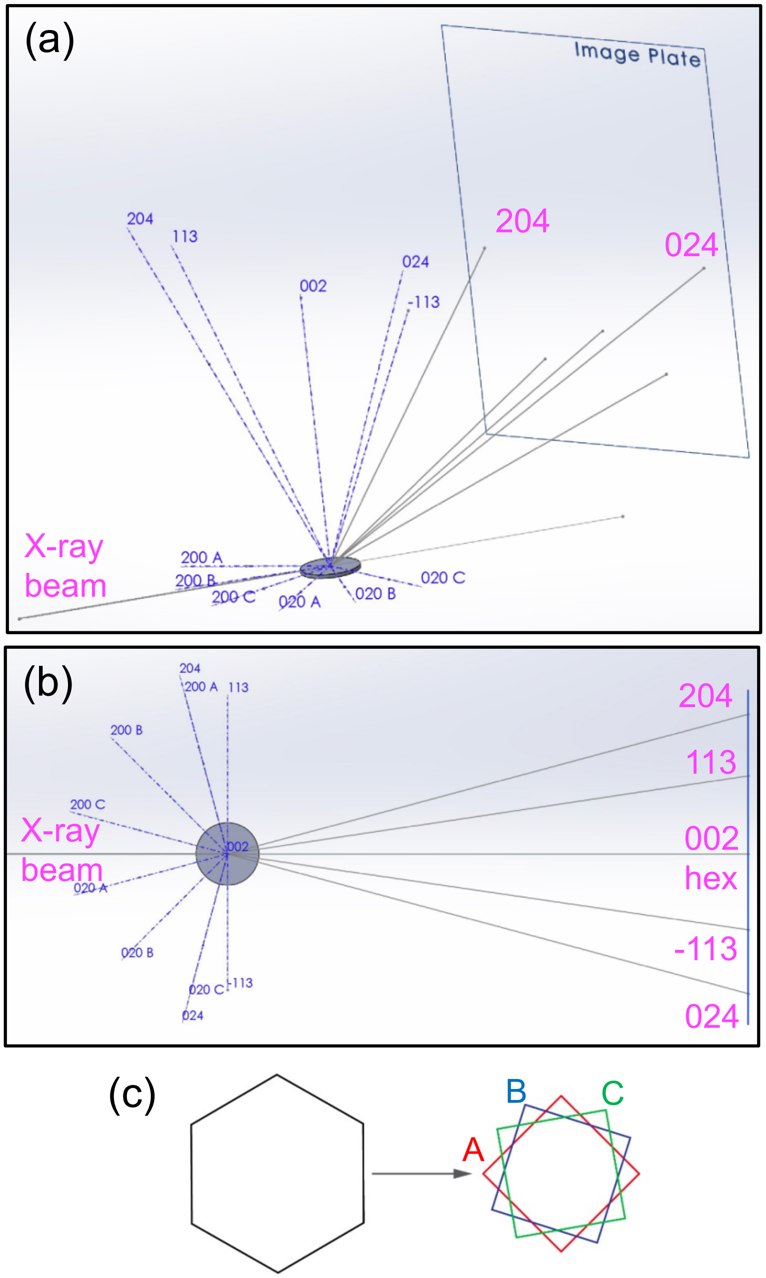

Figure 37. Thor Expt. No. 154: explanation for dynamic 204 fcc spots in the out-of-plane symmetric reflections through (a) the isometric view, (b) the view along the c-axis, and (c) the three orientations labelled as "A, "B", and "C". The 002 hex reflection indicates the location of the preshot-static Laue spot.

IV. SUMMARY

A novel, compact, pulsed x-ray diffraction diagnostic was implemented on ramp compression experiments on the Thor pulsed-power platform. Timing of the x-ray pulse during the ramp compression wave was confirmed. In addition, the effects of different x-ray windows on the dynamic XRD patterns were examined. Finally, the first successful XRD pattern exhibiting a dynamic phase transition on Thor was observed. The dynamic XRD pattern clearly showed signatures of the solid-solid phase transition of wurtzite-to-rocksalt structure in a ramp compressed single-crystal CdS sample.

ACKNOWLEDGEMENTS

Sandia National Laboratories is a multimission laboratory managed and operated by National Technology & Engineering Solutions of Sandia, LLC, a wholly owned subsidiary of Honeywell International Inc., for the U.S. Department of Energy's National Nuclear Security Administration under contract DE-NA0003525. This work was supported by the Sandia's Laboratory Directed Research & Development (LDRD) program.

This paper describes objective technical results and analysis. Any subjective views or opinions that might be expressed in the paper do not necessarily represent the views of the U.S. Department of Energy or the United States Government.

DATA AVAILABILITY

The data that support the findings of this study are available from the corresponding author upon reasonable request.

REFERENCES

1. J.-P. Davis, C. Deeney, M. D. Knudson, R. W. Lemke, T. D. Pointon, and D. E. Bliss, Phys. Plasmas **12**, 056310 (2005).
2. D. B. Sinars, M. A. Sweeney, C. S. Alexander, D. J. Ampleford, T. Ao, *et al.*, Phys. Plasmas **27**, 070501 (2020).
3. R. G. McQueen, S. P. Marsh, J. W. Taylor, J. N. Fritz and W. J. Carter, in High-Velocity Impact Phenomena, edited by R. Kinslow, pp. 249, Academic Press, New York, 1970.
4. R. J. Trainor, J. W. Shaner, J. M. Auerbach, and N. C. Holmes, Phys. Rev. Lett. **42**, 1154 (1979).
5. A. C. Mitchell and W. J. Nellis, J. Appl. Phys. **52**, 3363 (1981).
6. C. E. Ragan, Phys. Rev. A **29**, 1391 (1984).
7. D. B. Reisman, A. Toor, R. C. Cauble, C. A. Hall, J. R. Asay, M. D. Knudson, and M. D. Furnish, J. Appl. Phys. **89**, 1625 (2001).
8. C. A. Hall, J. R. Asay, M. D. Knudson, W. A. Stygar, R. B. Spielman, T. D. Pointon, D. B. Reisman, A. Toor, and R.C. Cauble, Rev. Sci. Instrum. **72**, 3587 (2001).
9. T. Ao, J. R. Asay, S. Chantrenne, M. R. Baer, and C. A. Hall, Rev. Sci. Instrum. **79**,

013903 (2008).

10. J. H. Nguyen, D. Orlikowski, F. H. Streitz, J. A. Moriarty, and N. C. Holmes, J. Appl. Phys. **100**, 023508 (2006).
11. R. F. Smith, J. H. Eggert, A. Jankowski, P. M. Celliers, M. J. Edwards, Y. M. Gupta, J. R. Asay, and G. W. Collins, Phys. Rev. Lett. **98**, 065701 (2007).
12. C. Kittel and P. McEuen, Introduction to Solid State Physics, 8th Edition (John Wiley & Sons, Inc, 1996).
13. N. F. M Henry and K. Lonsdale (Editors), International Tables for X-Ray Crystallography, Vol. 1, 2nd Edition, (Kynoch Press, Birmingham, England, 1965).
14. P. Debye and P. Scherrer, Physik. Z. **17**, 277 (1916).
15. A.W. Hull, Phys. Rev. **10**, 661 (1917).
16. P. Kalita, P. Specht, S. Root, N. Sinclair, A. Schuman, M. White, A. L. Cornelius, J. Smith, S. Sinogeikin, Phys. Rev. Lett. **119**, 255701 (2017).
17. S. J. Turneaure, S. M. Sharma, and Y. M. Gupta, Phys. Rev. Lett. **121**, 135701 (2018).
18. A. E. Gleason, C. A. Bolme, E. Galtier, H. J. Lee, E. Granados, D. H. Dolan, C. T. Seagle, T. Ao, S. Ali, A. Lazicki, D. Swift, P. Celliers, and W. L. Mao, Phys. Rev. Lett. **119**, 025701 (2017).

19. D. B. Reisman, B. S. Stoltzfus, W. A. Stygar, K. N. Austin, E. M. Waisman, R. J. Hickman, J.-P. Davis, T. A. Haill, M. D. Knudson, C. T. Seagle, J. L. Brown, D. A. Goerz, R. B. Spielman, J. A. Goldlust, and W. R. Cravey, Phys. Rev. ST Accel. Beams **18**, 090401 (2015).
20. D. V. Morgan, D. Macy, and G. Stevens., Rev. Sci. Instrum. **79**, 113904 (2008).
21. D. V. Morgan, M. Grover, D. Macy, M. Madlener, G. Stevens, and W.D. Turley, Powder Diffr. **25**, 138 (2010).
22. L. M. Barker and R. E. Hollenbach, J. Appl. Phys. **43**, 4669 (1972).
23. W. F. Hemsing, Rev. Sci. Instrum. **50**, 73 (1979).
24. O. T. Strand, D. R. Goosman, C. Martinez, and T. L. Whitworth, Rev. Sci. Instrum. **77**, 083108 (2006).
25. D. H. Dolan, Rev. Sci. Instrum. **81**, 53905 (2010).
26. Q. Johnson, A. Mitchell, R. Keeler, and L. Evans, Phys. Rev. Lett. **25**, 1099 (1970).
27. Y. M. Gupta, K. A. Zimmerman, P. A. Rigg, E. B. Zaretsky, D. M. Savage, and P. M. Bellamy, Rev. Sci. Instrum. **70**, 4008 (1999).
28. T. d'Almeida and Y. M. Gupta, Phys. Rev. Lett. **85**, 330 (2000).
29. D. G. Pellinen, M. S. Di Capua, S. E. Sampayan, H. Gerbracht, and M. Wang, Rev.

Sci. Instrum. **51**, 1535 (1980).

30. Y. Amemiyas and J. Miyahara, Nature **336**, 89 (1988).
31. S. G. Gales and C. D. Bentley, Rev. Sci. Instrum. **75**, 4001 (2004).
32. A. L. Meadowcroft, C. D. Bentley, and E. N. Stott, Rev. Sci. Instrum. **79**, 113102 (2008).
33. B. R. Maddox, H. S. Park, B. A. Remington, N. Izumi, S. Chen, C. Chen, G. Kimminau, Z. Ali, M. J. Haugh, and Q. Ma, Rev. Sci. Instrum. **82**, 023111 (2011).
34. J. H. Carpenter (private communication).
35. A. Robinson, T. Brunner, S. Carroll, R. Drake, C. Garasi, T. Gardiner, T. Haill, H. Hanshaw, D. Hensinger, D. Labreche, R. Lemke, E. Love, C. Luchini, S. Mosso, J. Niederhaus, C. Ober, S. Petney, W. Rider, G. Scovazzi, O. Strack, R. Summers, T. Trucano, V. Weirs, M. Wong, and T. Voth, "ALEGRA: An arbitrary Lagrangian-Eulerian multimaterial, multiphysics code," in 46th AIAA Aerospace Sciences Meeting and Exhibit, Aerospace Sciences Meetings, 2008.
36. R. W. Lemke, M. D. Knudson, D. E. Bliss, K. Cochrane, J.-P. Davis, A. A. Giunta, H. C. Harjes, and S. A. Slutz, J. Appl. Phys. **98**, 073530 (2005).
37. R. W. Lemke, M. D. Knudson, and J.-P. Davis, International Journal of Impact

Engineering **38**, 480 (2011).

38. A. Porwitzky and J. Brown, Phys. Plasmas **25**, 063102 (2018).
39. P. A. Rigg and Y. M. Gupta, Appl. Phys Lett. **73**, 1655 (1998).
40. P. W. Bridgman, Proc. Am. Acad. Arts Sci. **81**, 165 (1952).
41. J. C. Jamieson, Science 1**40**, 72 (1963).
42. H. Xia, S. J. Duclos, A. L. Ruoff, and Y. K. Vohra, Phys. Rev. Lett. **64**, 204 (1990).
43. R. G. McQueen, S. P. Marsh, J. W. Taylor, J. N. Fritz, and W. J. Carter, High Velocity Impact Phenomena, edited R. Kinslow (New York: Academic, 1970).
44. L. V. Al'tshuler, A. A. Bakanova, I. P. Dudoladov, E. A. Dynin, R. F. Trunin, and B. S. Chekin, J. Appl. Mech. Tech. Phys. **22**, 145 (1981).
45. C. W. Greeff, Modelling Simul. Mater. Sci. Eng. **13**, 1015 (2005).
46. A. R. Kutsar, M. N. Pavlovskii, and V. V. Kamissarov, JETP Lett. **39**, 480 (1984).
47. S. G. Song and G. T. Gray III, Phil. Mag. A **71**, 275 (1995).
48. P. Kalita, J. Brown, P. Specht, and S. Root, Phys. Rev. B **102**, 060101(R) (2020).
49. S. P. Lyon and J. P. Johnson, “SESAME: The Los Alamos National Laboratory Equation of State Database”, LANL Report LA-UR-92-3407 (1992).
50. M. D. Knudson, R. W. Lemke, D. B. Hayes, C. A. Hall, C. Deeney, and J. R. Asay,

J. Appl. Phys. **94**, 4420 (2003).

51. J.-P. Davis, J. Appl. Phys. **99**, 103512 (2006).
52. D. G. Hicks, P. M. Celliers, G.W. Collins, J. H. Eggert, and S. J. Moon, Phys. Rev. Lett. **91**, 035502 (2003).
53. L. E. Kirsch, S. J. Ali, D. E. Fratanduono, R. G. Kraus, D. G. Braun, A. Fernandez-Panella, R. F. Smith, J. M. McNaney, and J. H. Eggert, J. Appl. Phys. **125**, 175901 (2019).
54. M. D. Knudson, Y. M. Gupta, and A. B. Kunz, Phys. Rev. B **59**, 11704 (1999).
55. M. D. Knudson and Y. M. Gupta, Phys. Rev. Lett. **81**, 2938 (1998).
56. M. D. Knudson and Y. M. Gupta, J. Appl. Phys. **91**, 9561 (2002).
57. C. W. Greeff, J. Dyn. Behav. Mat. **2**, 452 (2016).
58. Z. P. Tang and Y.M. Gupta, J. Appl. Phys. **81**, 7203 (1997).
59. B. Li, J. Xu, W. Chen, D. Fan, Y. Kuang, Z. Ye, W. Zhou, and H. Xie, J. Alloys and Compounds **743**, 419 (2018).
60. J. J. Tan, Y. Li, and G. G. Ji, Acta Physica Polonica A **120**, 501 (2011).